Supplementary Information for

Hyperconjugation-Controlled Molecular Conformation Weakens Lithium-Ion Solvation and Stabilizes Lithium Metal Anode

Yuelang Chen[†1,2], Sheng-Lun Liao[†1], Huaxin Gong[1], Zewen Zhang[3], Zhuojun Huang[3], Sang Cheol Kim[3], Elizabeth Zhang[1,3], Hao Lyu[1], Weilai Yu[1], Yangju Lin[1], Philaphon Sayavong[2,3], Yi Cui*[3,4,5], Jian Qin*[1], Zhenan Bao*[1]

[1]Department of Chemical Engineering, Stanford University, Stanford, CA, USA.

[2]Department of Chemistry, Stanford University, Stanford, CA, USA.

[3]Department of Materials Science and Engineering, Stanford University, Stanford, CA, USA.

[4]Department of Energy Science and Engineering, Stanford University, Stanford, CA, USA.

[5]Stanford Institute for Materials and Energy Sciences, SLAC National Accelerator Laboratory, Menlo Park, CA, USA.

[†]Y.Chen and S.L. contributed equally to this work.

*Correspondence and request for materials should be addressed to Z.B. (email: zbao@stanford.edu), Y. Cui (email: yicui@stanford.edu), or J.Q. (email: jianq@stanford.edu)

1. Discussion on hyperconjugation:

The hyperconjugation occurs when the electron density in the nonbonding orbital on O (*n*) delocalizes into the empty C-O sigma antibonding orbital (σ^*) in the β position (Figure 1b), which stabilizes the molecule.[1] Such interaction constrains the spatial alignment of *n* and σ^* orbitals. As a result, *n* is anti and the methyl group is gauche to the neighboring C-O. There are two pairs of $n \rightarrow \sigma^*$ interactions per DMM or DEM, leading to the [gauche, gauche] conformation.[1,2,3]

2. Discussion on DFT calculations:

DFT is a common method to compare solvent binding ability with Li^+. For solvents with bidentate coordination with Li^+ (e.g. DME and DEE), the energies calculated from a Li^+-solvent pair offer a qualitative comparison for Lewis basicity of solvents.

In the case of DMM and DEM, the most stable molecular geometry is [gauche, gauche]. Based on chemical intuition, we expect monodentate coordination. However, the optimization of a Li^+-solvent pair by DFT results in bidentate chelation. This is because a Li^+-solvent pair is highly positively charged due to undercoordination, and the system must minimize energy by donating electron densities from all Lewis basic centers on the solvent to the Li^+ regardless of molecular geometry. In the real system, however, the ion distribution satisfies Poisson–Boltzmann equation and gives rise to a relatively stable sheath structure. Therefore, for our purpose of determining molecular geometry of DMM and DEM when coordinated to Li^+, we need to carry out DFT on a complete Li^+ solvation shell.

3. Discussion on the limitation of MD simulation:

The average denticity predicted by MD simulation in Figure 2d has two limitations. First, molecular orbitals are not considered, and electron densities are approximated as point charges on each atom. This means the orientation of electron density on DMM and DEM (Figure 1a) are ignored. Second, DMM and DEM are relatively small molecules with two oxygens close to each other. The thermal fluctuation could make the non-coordinating oxygen enter the cutoff distance (see Method). Therefore, the calculated average denticity of DMM and DEM is likely overestimated.

4. Discussion on the ionic conductivity:

Ionic conductivity (σ) is an important consideration for designing practical electrolytes.[4] We investigate the effect of ion concentration on σ, which is less explored especially for the weakly solvating electrolytes commonly used for LMBs. The common LIB electrolytes exhibit peak σ at around 1 M, which implies that an expected drawback of HCEs is the decrease of σ with concentration. Interestingly, as the solvation ability of solvent weakens (DME > DEE > DMM > DEM, Figure 2), the σ peaks at higher LiFSI concentrations (Figure S13a,b). Furthermore, the molar conductivities (Λ) of DMM and DEM electrolytes peak at around 1.7 M, whereas that of DME and DEE electrolytes do not show a peak above 0.9 M (Figure S13c, d). Notably, in both DMM and DEM, 1.7 M and 2.4 M electrolytes have higher Λ than 0.9 M electrolytes, which indicates that ion transport is faster despite higher viscosity in more concentrated solutions, and that the initial increase in σ is not solely due to increased charge carrier concentration. The observed trend in σ and Λ indicates that ion transport is not necessarily slowed by increased ion pairing and aggregation in weakly solvating, high-concentration electrolytes. Although structural diffusion (i.e. ion diffusion through the exchange of solvation shell) has been proposed for ion transport in HCEs[5,6,7], the factors and mechanisms that determine the rate of transport remain elusive. We will further investigate this topic in a separate publication. Overall, the σ of 3 M LiFSI / DMM is similar to 3 M

LiFSI / DME and DEE, and is higher than 1.5 M LiFSI-1.2DME-3TTE and 1.2 M LiFSI / F4DEE and F5DEE (Table S3). In contrast, 3 M LiFSI / DEM has a low σ, which limits the high-rate capability and stability.

5. Discussion on Li||Li cell impedance with cycle life:

The contributions to overpotential were investigated by electrochemical impedance spectroscopy (EIS) on Li||Li cells after every 120 cycles at 1 mA cm^{-2} and 1 mAh cm^{-2} (Figure S15). Throughout cycling, the bulk electrolyte resistance (R_{bulk}) remained stable in all three electrolytes. The interfacial resistance ($R_{interface}$) continuously increased in 3 M LiFSI / DEM, whereas $R_{interface}$ remained stable in 3 M LiFSI / DMM and DEE after the initial decrease. Since the exchange current density of Li redox reaction is significantly higher than 1 mA cm^{-2} at room temperature, the contribution from charge transfer resistance to $R_{interface}$ should be small.[8] Therefore, the quick increase in $R_{interface}$ and Li||Li overpotential in 3 M LiFSI / DEM was attributed to SEI instability. Both R_{bulk} and $R_{interface}$ were slightly higher in 3 M LiFSI / DMM than in 3 M LiFSI / DEE after cycling despite that the overpotential in 3 M LiFSI / DMM was lower. This was due to the significantly higher t_+ in 3 M LiFSI / DMM than in 3 M LiFSI / DEE (Table S3). Notably, in 3 M LiFSI / DEM, the high t_+ was not sufficient to compensate for the large R_{bulk} and $R_{interface}$ in the later cycles, leading to the highest overpotential.

6. Discussion on the limiting factors for cycle life in our Li||LFP cells:

With 50 μm thick Li, the cycle life was limited by increase in overpotential, as evidenced by the lack of voltage divergence at the end of charge of the 250th and 150th cycle (roughly corresponding to 80% capacity retention) in 3 M LiFSI / DMM and 3 M LiFSI / DEM respectively (Figure S21a-b and S22a-b). As a result, 3 M LiFSI / DMM with a slower increase in overpotential outperformed 3 M LiFSI / DEM (Figure 5e,

f). With 20 µm thick Li, the voltage divergence at the end of charge remained visible at the 200th and 150th cycle (roughly corresponding to 80% capacity retention) in 3 M LiFSI / DMM and 3 M LiFSI / DEM respectively (Figure S21c and S22c), which indicated that Li inventory consumption likely limited cycle life. Consequently, 3 M LiFSI / DMM with higher initial CE and stabilized CE outperformed 3 M LiFSI / DEM (Figure 5g).

7. Discussion on SEI property and electrode morphology:

To understand the origin of faster activation and higher CE in Li||Cu in the order of 3 M LiFSI / DMM > DEM > DEE (Figure 3a), we characterized their SEI. Cryogenic transmission electron microscopy (cryo-TEM) was used to visualize the structure of SEI in the dry state after a one-step electrochemical deposition of Li on Cu grid.[9,10] The SEI formed in both DMM and DEM electrolytes was around 13 nm compared to 8 nm in the DEE electrolyte (Figure S23a-c, S24). Here, we observed a loose connection between thicker SEI and faster CE activation. However, it is worth noting that the correlation between SEI thickness and Li CE remains inconclusive in the literature.[11,12,9,13,14] In addition, the elemental compositions of SEI were measured by energy-dispersive X-ray spectroscopy (cryo-EDS). The relative contributions from LiFSI and solvent decomposition were characterized by F/C, S/C, and N/C ratios (Figure S23d), all of which decreased in the order of DEE >> DMM > DEM (indicating increasing content of organic SEI), commensurate with the trend in SEI thickness (DEE << DMM < DEM). The atomic ratios were further characterized by XPS after 10 cycles at 0.5 mA cm^{-2} and 1 mAh cm^{-2} in Li||Cu cells. The O/C, F/C, S/C and N/C ratios decreased in the order of DEE>>DMM≈DEM (Figure S25a), which confirmed the acetal electrolytes formed more organic-rich SEI. Notably, despite the differences in atomic ratios, the SEI species were very similar for all three electrolytes (Figure S25b-d). Previous work demonstrated that the electrolytes with high CE (>99%) typically formed more inorganic-rich SEI compared to those with

low CE (<90%).[15,16,17,18] However, such correlation was unclear when comparing electrolytes with small differences in CE in this work and previous reports[16,19].

We imaged the initial Li deposition morphology on flat Cu substrate (0.5 mA cm^{-2}, 0.5 mAh cm^{-2}) by scanning electron microscopy (SEM), which showed no obvious difference among the three electrolytes (Figure S26-28) likely due to their small differences in CE. We further attempted to identify the origin of fast CE activation by residual SEI (rSEI) structure.[4,20] We prepared the cross sections of rSEI formed on Cu (same Li||Cu as Figure 3a, 0.5 mA cm^{-2} and 1 mAh cm^{-2} for 10 cycles) by focused ion beam (FIB) for SEM imaging. Highly porous rSEI structures were formed in both 3 M LiFSI / DMM and DEE (Figure S23e-f, S29), which was consistent with our previous observations on weakly solvating LiFSI-based electrolytes. [4,20] However, no significant difference in rSEI was observed despite ~1% difference in CE in the first 10 cycles (Figure 3a).

The Li deposition morphology in the presence of rSEI was characterized. The rSEI was formed on Cu (same Li||Cu as Figure 3a, 0.5 mA cm^{-2} and 1 mAh cm^{-2} for 10 cycles), followed by Li deposition for 0.1 to 1 mAh cm^{-2} (Figure S30). At 0.1 mAh cm^{-2}, Li already reached the top of rSEI at dispersed locations for all three electrolytes. At 0.5 mAh cm^{-2}, the DEE electrolyte showed more uniform distribution of Li nuclei and smaller aggregates of Li grains, whereas the DMM and DEM electrolytes showed more localized aggregates of Li grains coalesced together, which could reduce Li surface area. At 1 mAh cm^{-2}, the difference among the three electrolytes became less apparent as most surface was covered by deposited Li. Overall, it is possible that the lower initial Li||Cu CE in the DEE electrolyte (Figure 3a) was due to higher surface area of Li especially during the middle of deposition process. To better represent the practical cycling conditions, the Li and rSEI morphology was characterized on 50 μm thin Li. The rSEI was formed by 10 cycles at 0.4 mA cm^{-2} (Figure S31) or 4 mA cm^{-2} (Figure S32) plating current and 4 mA cm^{-2} stripping current for 4 mAh cm^{-2} in each step. The final deposition capacities were between 0.2 and 4 mAh cm^{-2}. At 0.4 mA cm^{-2} plating current, bulky Li grains first grew within the porous rSEI structure

before reaching the top of rSEI (Figure S31), similar to our previous report.[4] After 4 mAh cm^{-2} capacity, the DEE electrolyte showed almost complete coverage of Li grains on top of rSEI, whereas rSEI remained visible around protruding Li grains in the DMM and DEM electrolytes (Figure S31). This could indicate a higher capacity of Li hosted by rSEI in the acetal electrolytes.

When increasing plating current to 4 mA cm^{-2}, the rSEI appeared more compact (Figure S32), consistent with our previous observations.[4] However, compared to fluorinated ether electrolytes[4], the rSEI formed in this work could host slightly more Li capacity as evidenced by the lack of protruding Li grains at 0.2 mAh cm^{-2} (Figure S32). We attribute this difference to higher ionic conductivities and transport numbers of the electrolytes in this work.[4] At 1 mAh cm^{-2}, the lower-conductivity DEM electrolyte showed significantly more Li deposition on top of rSEI compared to the higher-conductivity DMM and DEE electrolytes (Figure S32), further validating the importance of ion transport on Li and rSEI morphology at high current densities.[4] At 4 mAh cm^{-2}, the electrode surface was covered by Li, with minimal differences among the three electrolytes (Figure S32).

Table S1. Concentrations of the various electrolytes investigated in this work. The molarities were calculated using electrolyte densities (see Table S3).

	Molarity (M, mol/L)	**Molality (m, mol/kg)**
1 mol LiFSI / liter DME	0.93	1.15
4 mol LiFSI / liter DME	3.08	4.61
1 mol LiFSI / liter DEE	0.94	1.19
4 mol LiFSI / liter DEE	3.06	4.75
1 mol LiFSI / liter DMM	0.94	1.16
4 mol LiFSI / liter DMM	3.08	4.65
1 mol LiFSI / liter DEM	0.89	1.20
4 mol LiFSI / liter DEM	2.97	4.81

Table S2. Li^+ self-diffusion coefficients calculated by MD simulation and measured by DOSY-NMR. The ion charge scaling factors in MD simulation are listed.

Li^+ self-diffusion coefficients (10^{-6} cm^2 s^{-1})	**MD**	**DOSY**	**Error (%)**	**MD scaling factor**
1 mol LiFSI / liter DME	7.89	5.94	+33	0.6
4 mol LiFSI / liter DME	0.727	0.544	+34	0.7
1 mol LiFSI / liter DEE	4.01	4.19	-4.3	0.6
4 mol LiFSI / liter DEE	0.604	0.507	+19	0.65
1 mol LiFSI / liter DMM	6.89	7.19	-4.2	0.65
4 mol LiFSI / liter DMM	0.975	0.992	-1.7	0.72
1 mol LiFSI / liter DEM	3.97	5.51	-28	0.6
4 mol LiFSI / liter DEM	0.684	0.592	+16	0.65

Table S3. Comparison of density, viscosity, ionic conductivity, and transport number.

	Solvent Density [a] (g/mL)	**Electrolyte Density [b] (g/mL)**	**Viscosity [c] (cp)**	**Ionic Conductivity [b] (mS cm^{-1})**	**Transport Number [d] (t_+)**
1 mol LiFSI / liter DME (~0.9 M)	0.867	0.975	1.44	23.4	0.29
4 mol LiFSI / liter DME (~3 M)	0.867	1.242	16.2	10.1	0.19
1 mol LiFSI / liter DEE (~0.9 M)	0.842	0.963	1.50	11.0	0.39
4 mol LiFSI / liter DEE (~3 M)	0.842	1.216	21.9	8.11	0.30
1 mol LiFSI / liter DMM (~0.9 M)	0.86	0.985	0.764	2.93	0.48
4 mol LiFSI / liter DMM (~3 M)	0.86	1.240	10.1	8.03	0.46
1 mol LiFSI / liter DEM (~0.9 M)	0.831	0.910	0.853	0.884	0.71
4 mol LiFSI / liter DEM (~3 M)	0.831	1.172	16.3	2.73	0.57
1.2 M LiFSI / F4DEE [11]	1.24	1.38	6.97	4.76	0.23
1.2 M LiFSI / F5DEE [11]	1.29	1.42	3.39	5.01	0.40
LiFSI-1.2DME-3TTE [16] (~1.5 M)	DME: 0.867 TTE: 1.53	1.454	4.8 (30°C)	2.44 (30°C)	0.29

[a] From Sigma or Synquest

[b] measured at room temperature unless indicated otherwise

[c] measured at 25°C unless indicated otherwise

[d] measured by Vincent-Bruce method at room temperature

Table S4. Commercial pouch cell parameters

Cu foil	7 µm
separator	12 µm PE coated with alumina
Al foil	12 µm
LFP : carbon : binder	96.7 : 1.5 : 1.8
Nominal capacity	~210 mAh
Areal capacity	~2.1 mAh cm^{-2}
Electrolyte	0.5 mL
Temperature	Uncontrolled room temperature
Pressure	~1000 kPa

Note: the only difference between these pouch cells and the Cu||LFP pouch cells used in ref[11] is the absence of 1 µm carbon coating on Cu here.

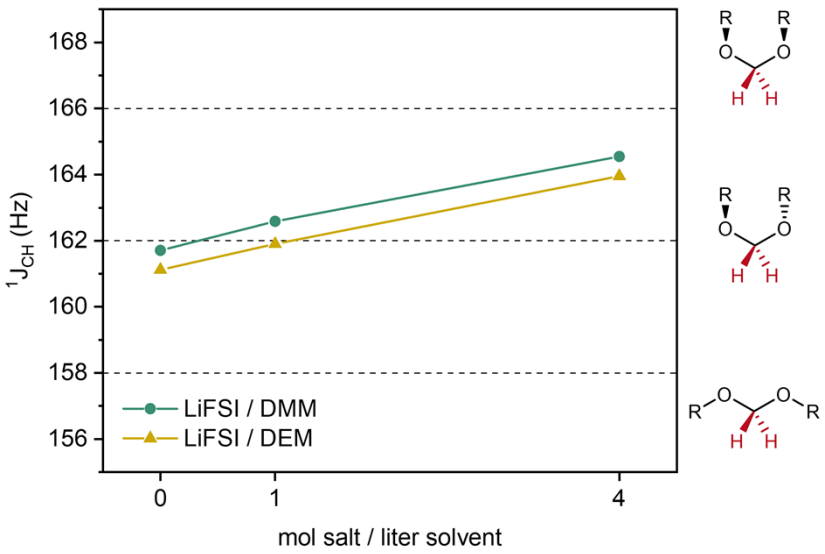

Figure S1. $^1J_{CH}$ coupling constants of anomeric -CH_2- of DMM and DEM with various concentrations of LiFSI. The corresponding molecular geometries for different ranges of $^1J_{CH}$ are shown on the right. The anomeric position is indicated in red.

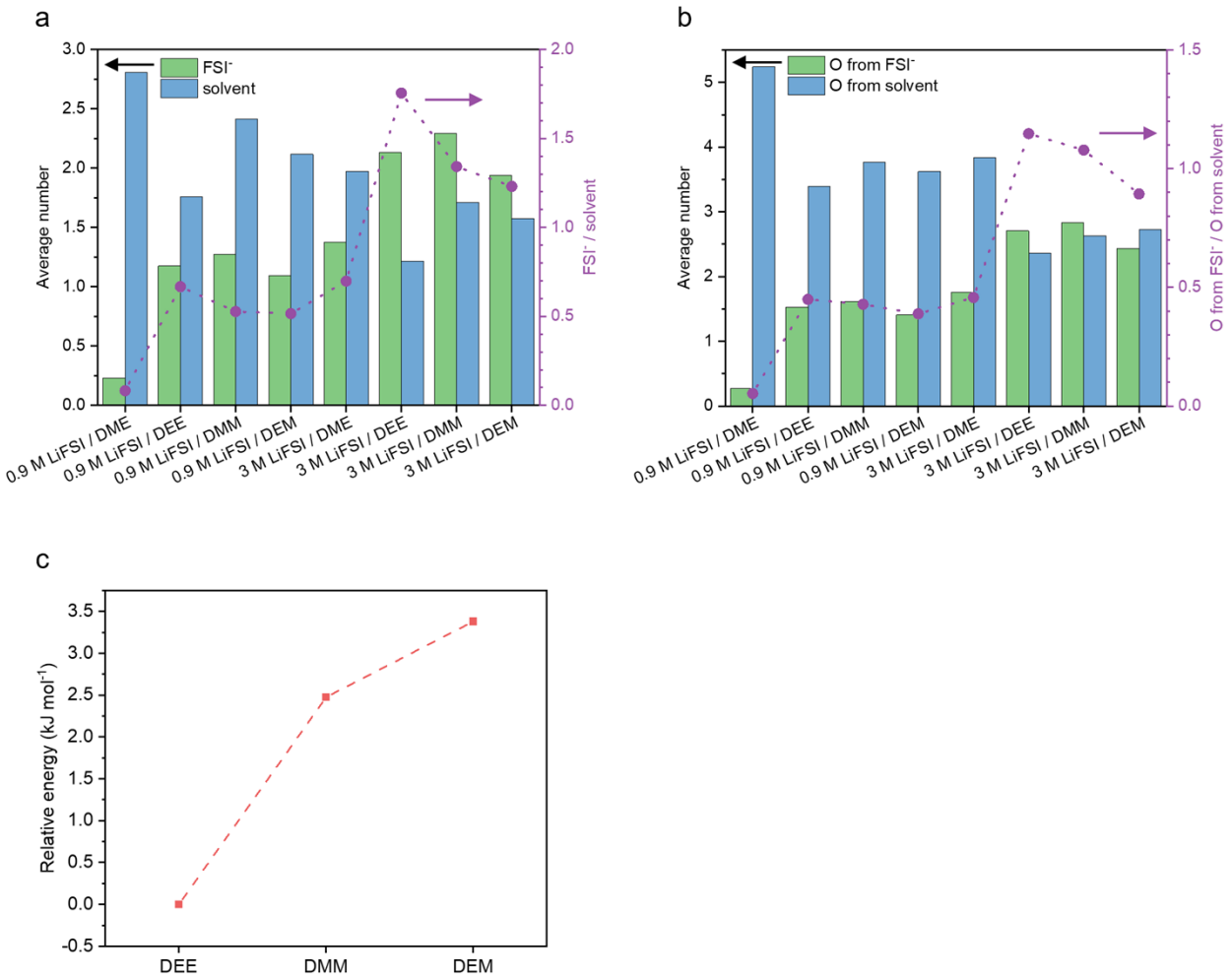

Figure S2. (a-b) MD simulation on solvation structures. (a) Average number of FSI^- and solvent in the inner solvation shell of Li^+ (green and blue bars, left axis), and their FSI^-/solvent ratio (purple, right axis). The number of solvent molecules and FSI^- anions were counted irrespective of denticity. (b) Average number of oxygens from FSI^- and solvent coordinating with Li^+ (green and blue bars, left axis), and their ratio (purple, right axis). Here, the denticity was taken into account. (c) DFT calculations on the relative difference in enthalpic interaction between LiFSI and various solvents. The ground state energy difference between a solvation complex (1 Li^+, 2FSI^-, 1 solvent) and a solvent molecule was calculated for DEE ,DMM, and DEM. The relative difference of this calculated value among DEE, DMM, and DEM indicated the relative enthalpic interaction between salt and different solvents.

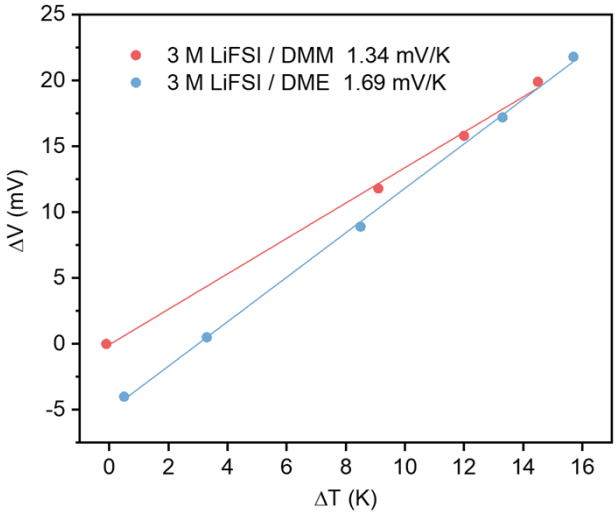

Figure S3. Non-isothermal measurement of electrode potential temperature coefficients (α).[21] The voltage response of Li||Li symmetric cell with asymmetric heating was recorded. The temperature coefficients were obtained from linear fitting. The entropy change of Li^+/Li half-cell reaction is related to temperature coefficient through $\Delta S = \alpha F$.

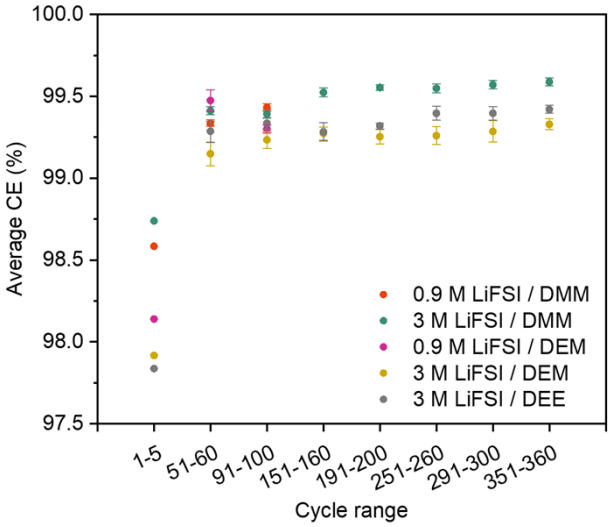

Figure S4. Average CE during various stages of Li||Cu cycling in Figure 3a, b. The error bars represent standard deviations.

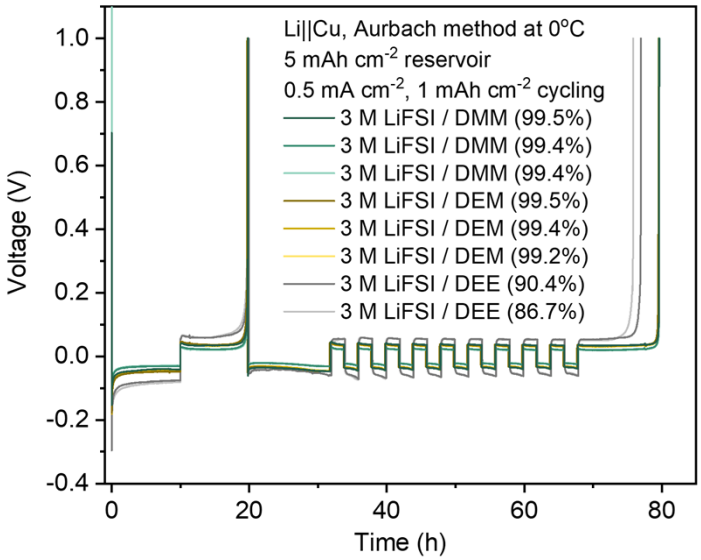

Figure S5. Li||Cu CE of 3 M LiFSI in DMM, DEM and DEE measured by the modified Aurbach method[22] at 0°C. Multiple cells are shown for each electrolyte.

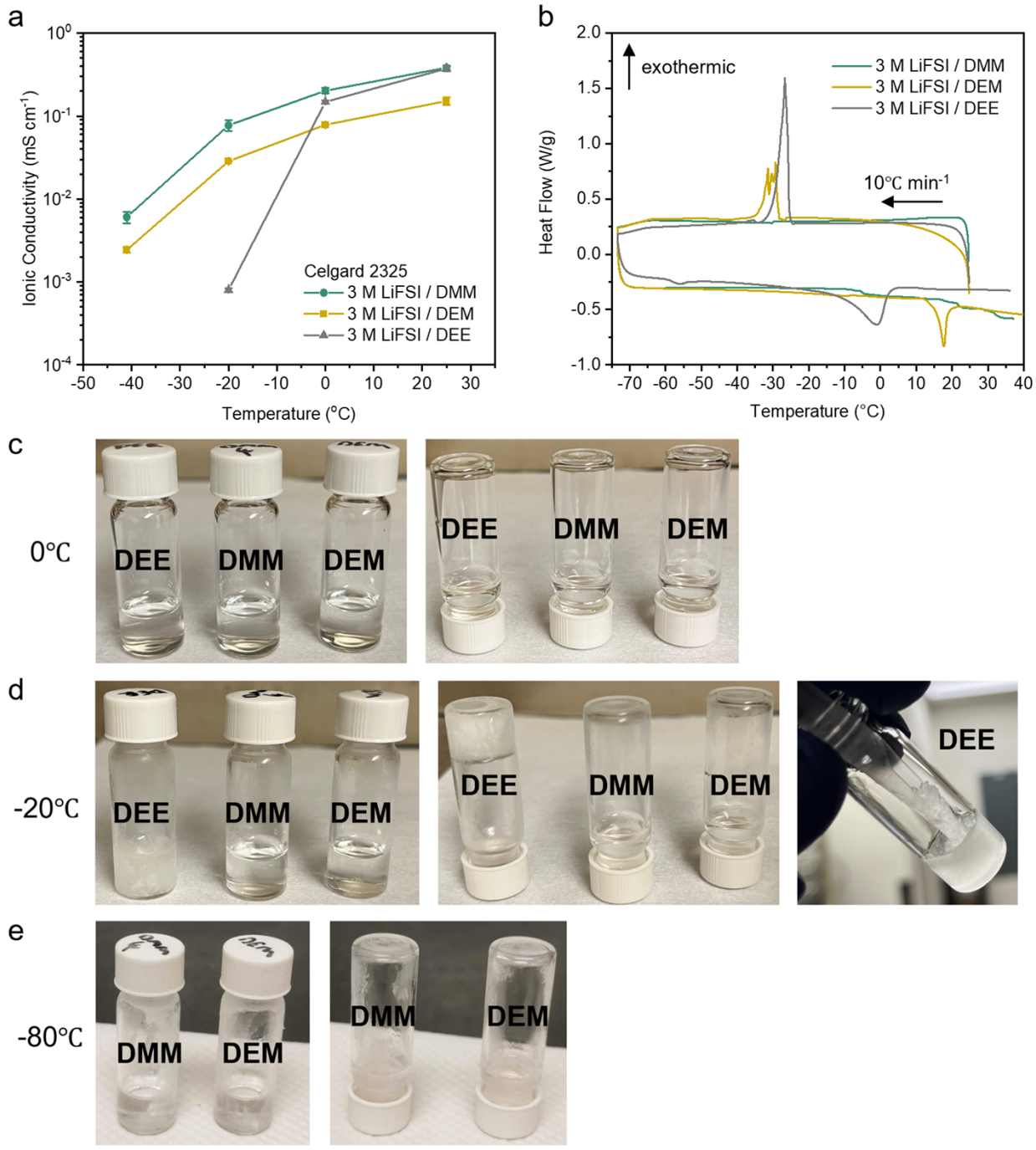

Figure S6. (a) Temperature-dependent ionic conductivities of 3 M LiFSI in DMM, DEM and DEE with Celgard 2325 separator. Three measurements were averaged for each point. The error bars represent standard deviations. (b) DSC measurement of the three electrolytes. (c-e) Pictures showing the physical state of 3 M LiFSI / DEE, DMM and DEM at (c) 0℃, (d) -20℃ and (e) -80℃.

Both the DMM and DEM electrolytes showed a gradual decrease in ionic conductivity from 25 to -41℃, whereas the DEE electrolyte showed a sharp decrease from 0 to -20℃ (Figure S6a). To explain this

difference, we probed the liquid-solid phase transition of these electrolytes. The DEE and DEM electrolytes showed onsets of exothermic peaks at -25°C and -28°C respectively during cooling, and their corresponding onsets of endothermic peaks at -10°C and 12°C respectively during heating (Figure S6b). In contrast, the DMM electrolyte showed no peak between 25°C and -75°C. The physical state of these electrolytes was observed after equilibrating for at least 2 hours at various temperatures (Figure S6c-e). The DEE electrolyte solidified at -20°C while the DMM and DEM electrolytes remained liquid at -80°C. Interestingly, despite the pair of endo- and exothermic peaks of the DEM electrolyte by DSC, the electrolyte remained liquid. Overall, the sharp drop in ionic conductivity of the DEE electrolyte was attributed to the liquid-solid transition, which was absent in the DMM and DEM electrolytes. Notably, the melting points of the pure solvents decrease in the order of DEM (-66°C), DEE (-74°C) and DMM (-105°C). Despite the intermediate melting point of DEE, 3 M LiFSI / DEE showed the highest liquidus temperature, indicating the impact of salt-solvent interactions on electrolyte phase.

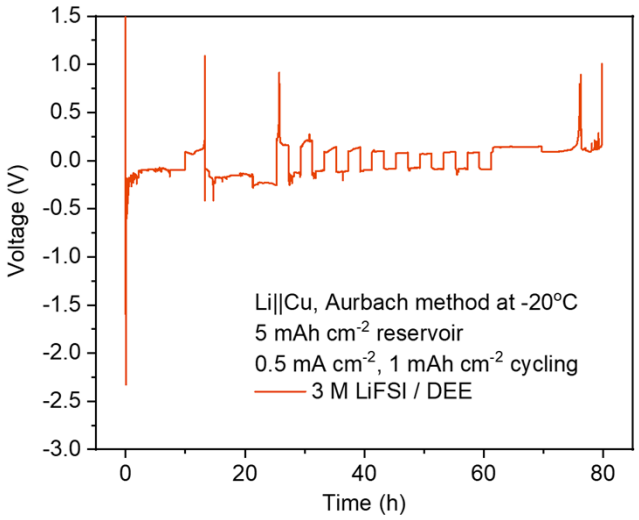

Figure S7. Li||Cu CE measurement of 3 M LiFSI in DEE by the modified Aurbach method[22] at -20℃.

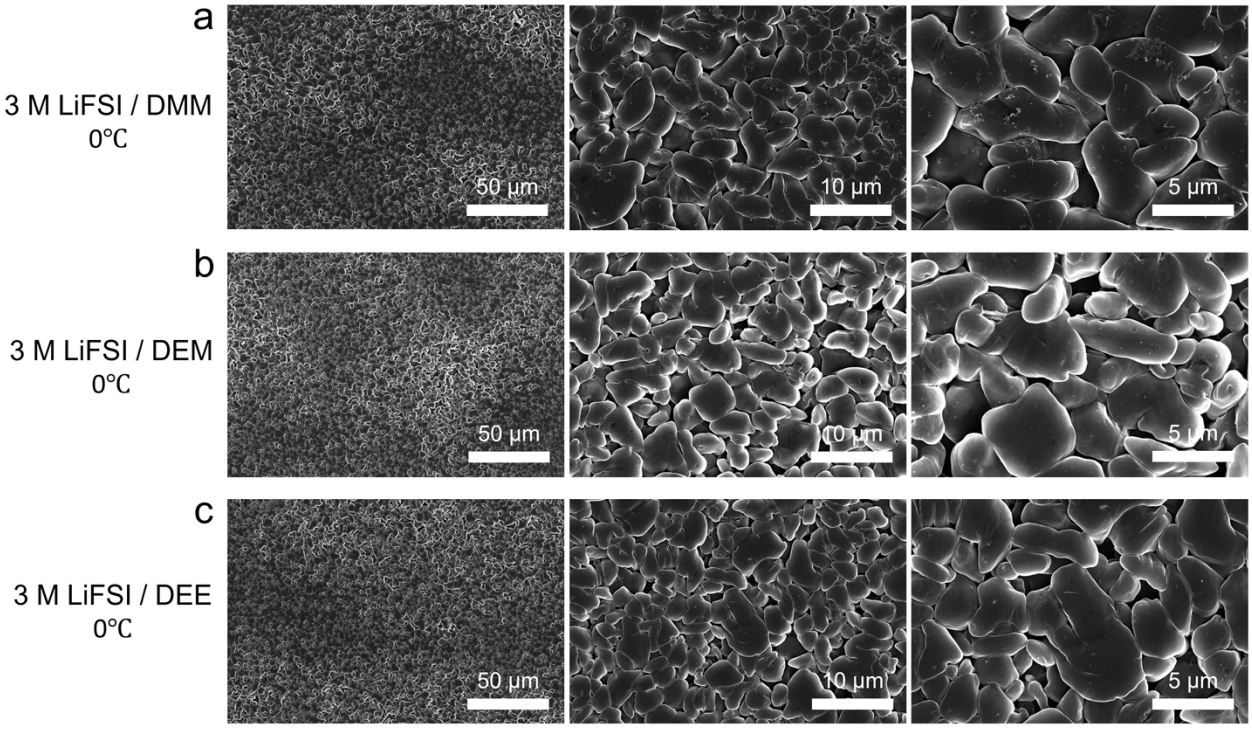

Figure S8. First-cycle Li deposition morphology on Cu at 0℃ (0.5 mA cm^{-2}, 5 mAh cm^{-2}).

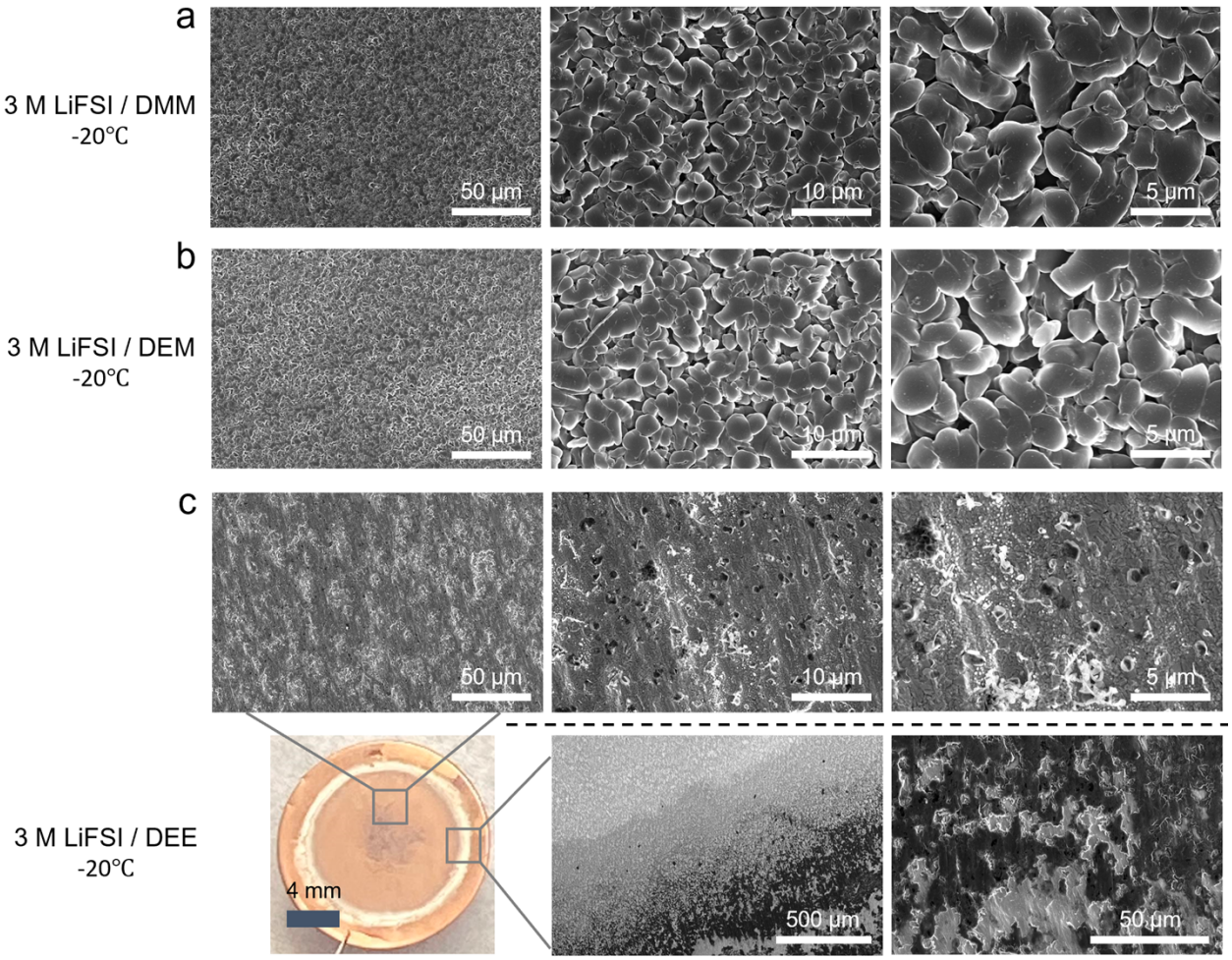

Figure S9. First-cycle Li deposition morphology on Cu at -20℃ (0.5 mA cm^{-2}, 5 mAh cm^{-2}). For the DEE electrolyte (c), there was minimal Li deposition in the middle of the electrode (top row). Only a small amount of Li was found near the edge (bottom row), which likely originated from the enhanced electric field at the edge of Li counter electrode.

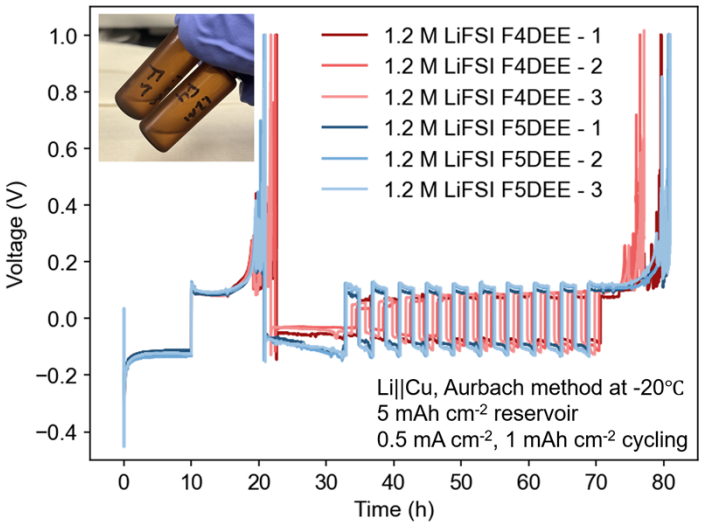

Figure S10. Li||Cu CE measurement of 1.2 M LiFSI in F4DEE and F5DEE by the modified Aurbach method at -20℃. Three repeated cells are shown for each electrolyte. The inserted photo shows that both electrolytes remained liquid at -20℃.

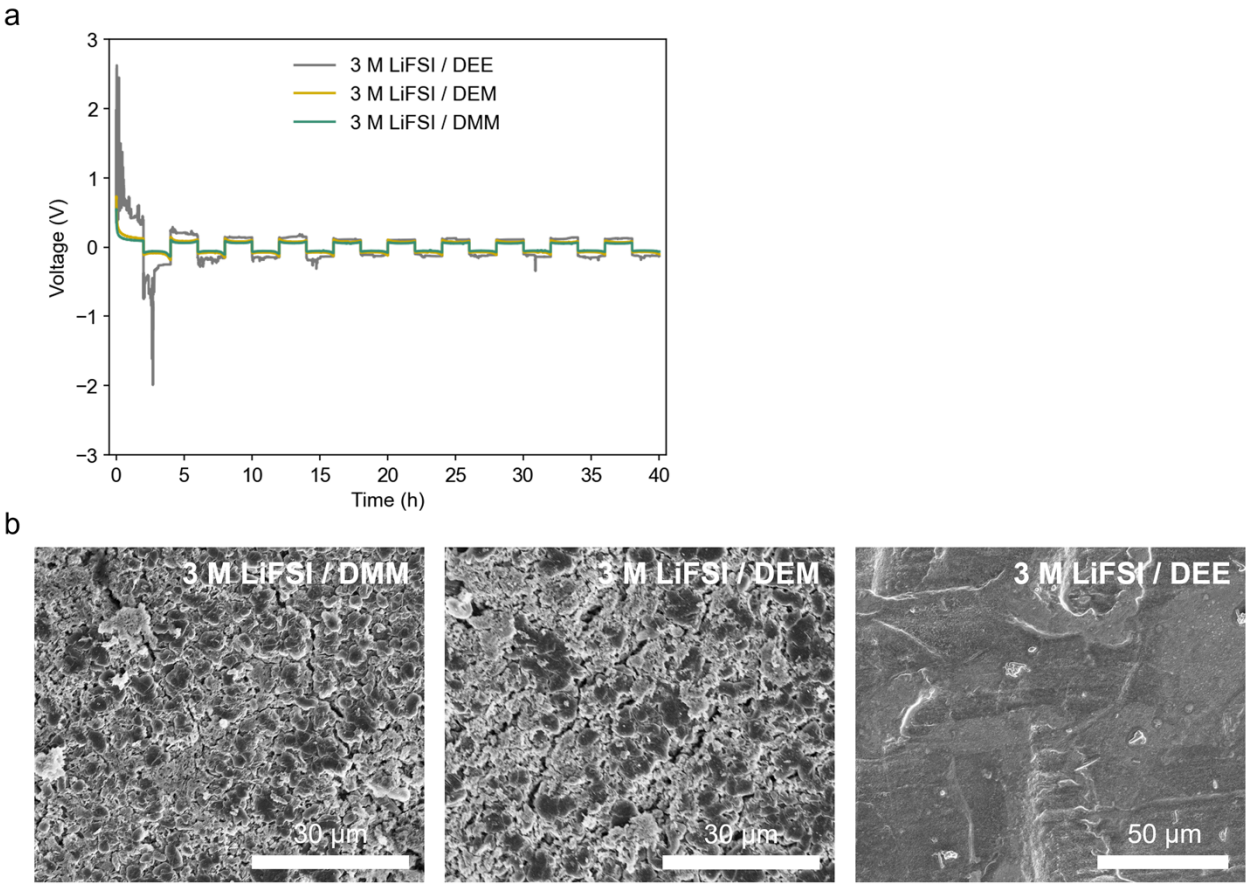

Figure S11. Li||Li cells cycled at -20°C at 0.5 mA cm^{-2}, 1 mAh cm^{-2} in various electrolytes. (a) Cell voltage. (b) SEM images of cycled Li electrodes (positive side).

To mimic the low-temperature operation of LMBs, we investigated Li cycling on Li (Figure S11) instead of Cu (Figure S8-9). At -20°C, 3 M LiFSI / DEE did not sustain stable cycling as evidenced by the spiky voltage, whereas the cycling was stable in 3 M LiFSI / DMM and DEM (Figure S11a). SEM images of the cycled Li electrode revealed virtually pristine Li surface in DEE, in contrast to the electrochemically deposited Li grains in DMM and DEM (Figure S11b). The observations were consistent between Li and Cu substrates.

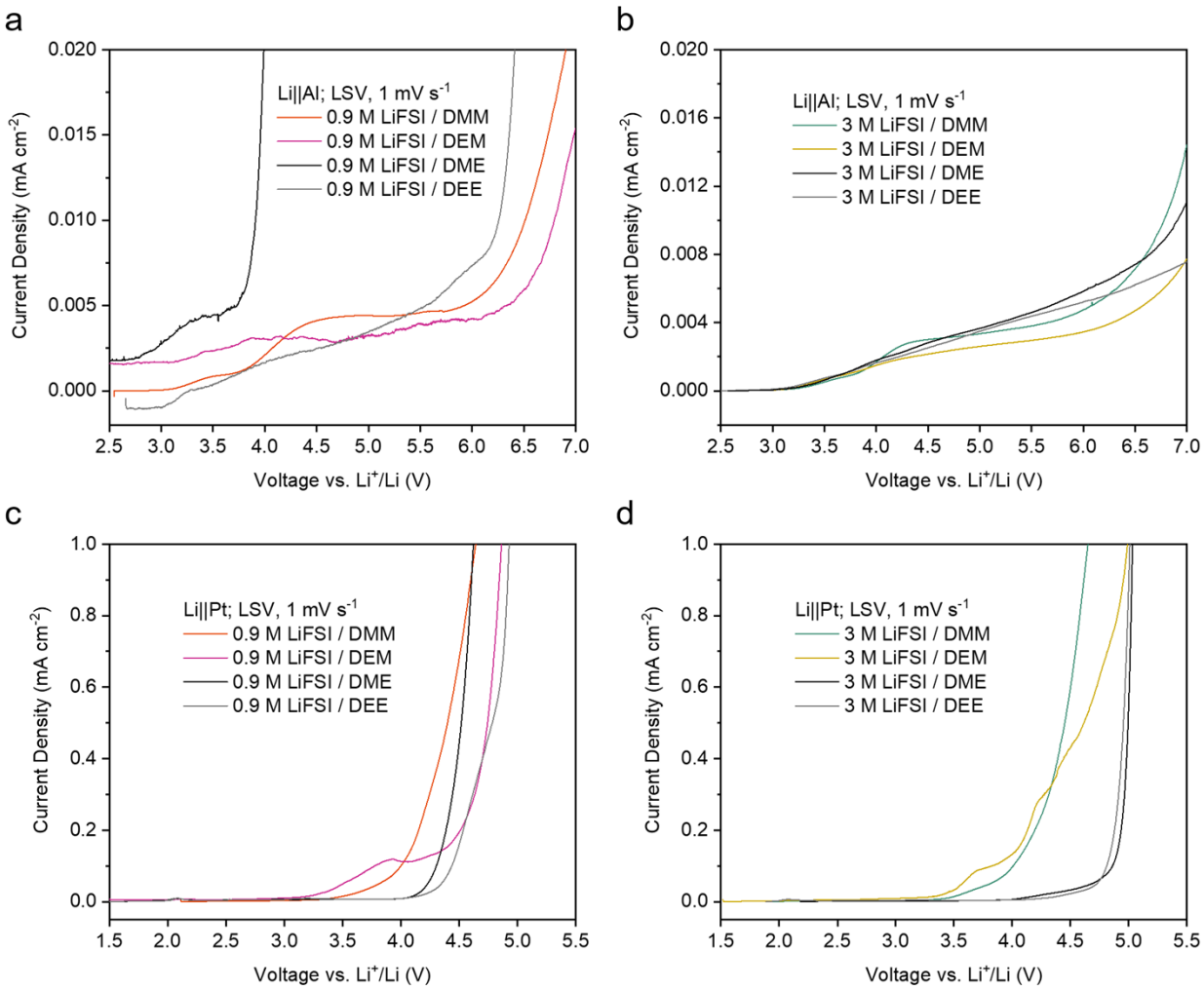

Figure S12. Oxidative stability of the electrolytes measured by LSV using Al (a-b) and Pt (c-d) as the working electrode. For comparison, the data of DME and DEE electrolytes are reproduced from ref [23].

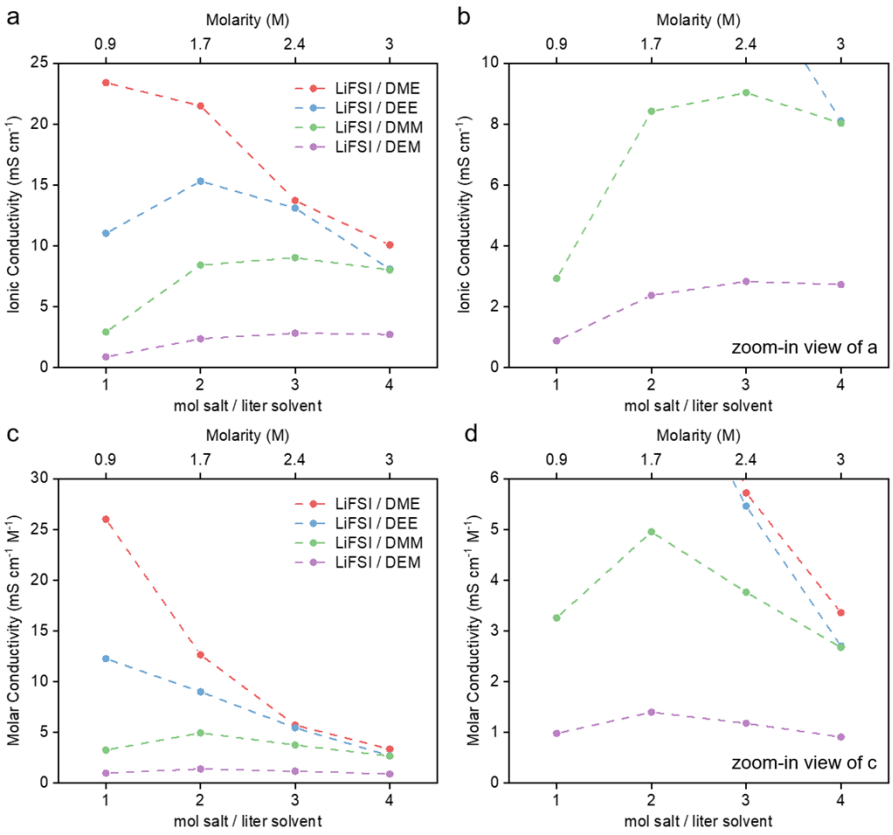

Figure S13. Concentration-dependent ionic conductivities (a-b) and molar conductivities (c-d) measured by EIS. The right panels are the zoom-in views of the left panels.

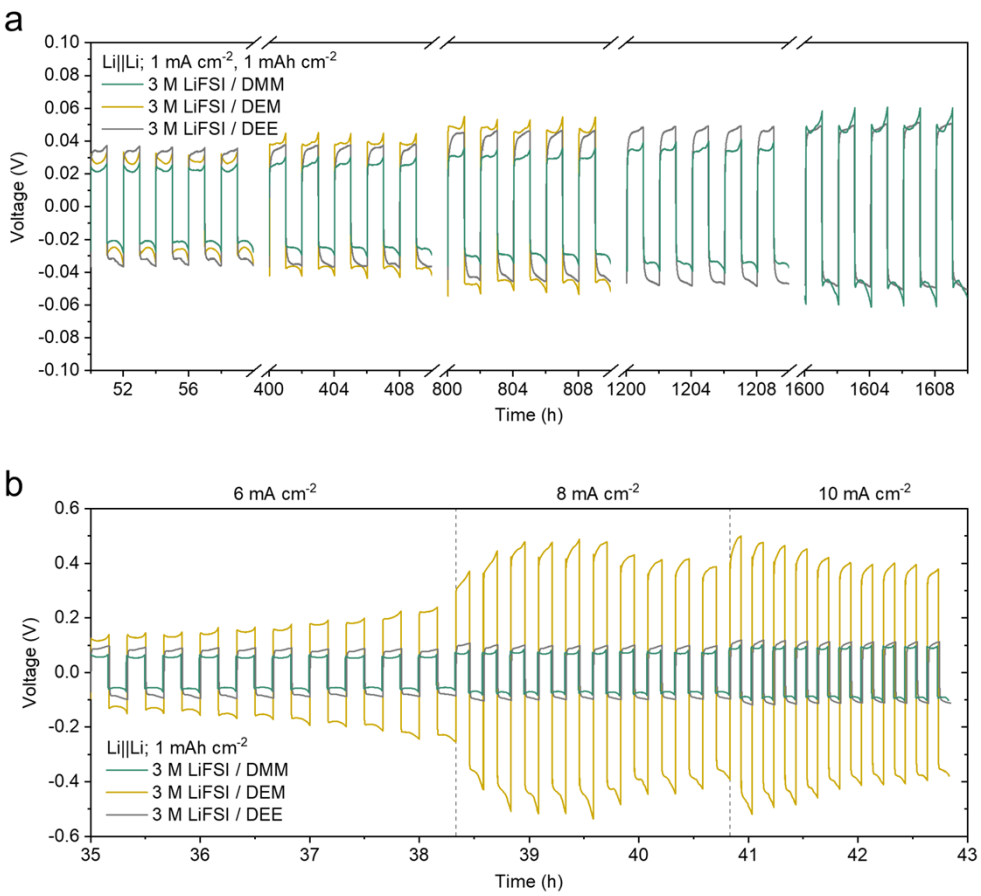

Figure S14. (a) Zoomed-in view of Figure 4a showing overpotential at different stages of Li||Li cycling. (b) Zoomed-in view of Figure 4b showing overpotential under high current densities.

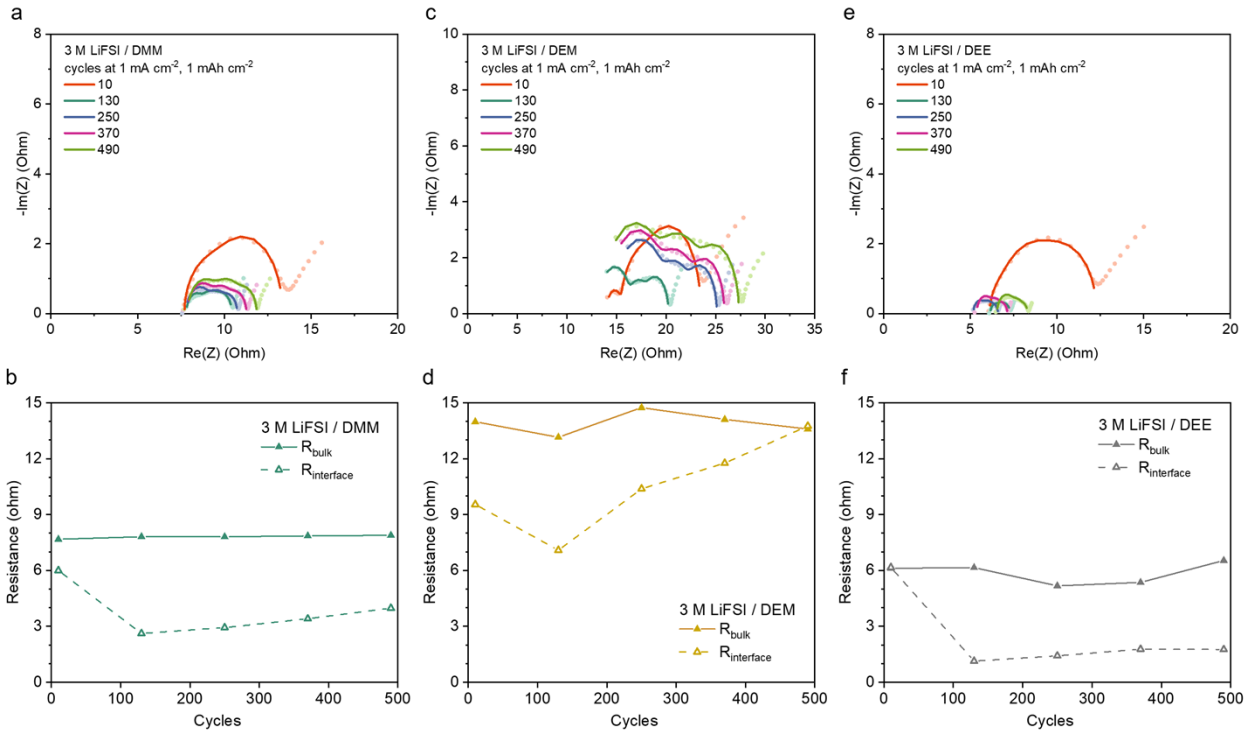

Figure S15. Impedance of Li||Li cells over cycling with 3 M LiFSI in DMM (a, b), DEM (c, d) and DEE (e, f). (a, c, e) Nyquist plots and fitting curves. An equivalent circuit of (R1+C2/R2+C3/R3+C4/R4) was used. (b, d, f) The corresponding fitting values for each electrolyte, where R_{bulk}=R1 and $R_{interface}$=R2+R3+R4.

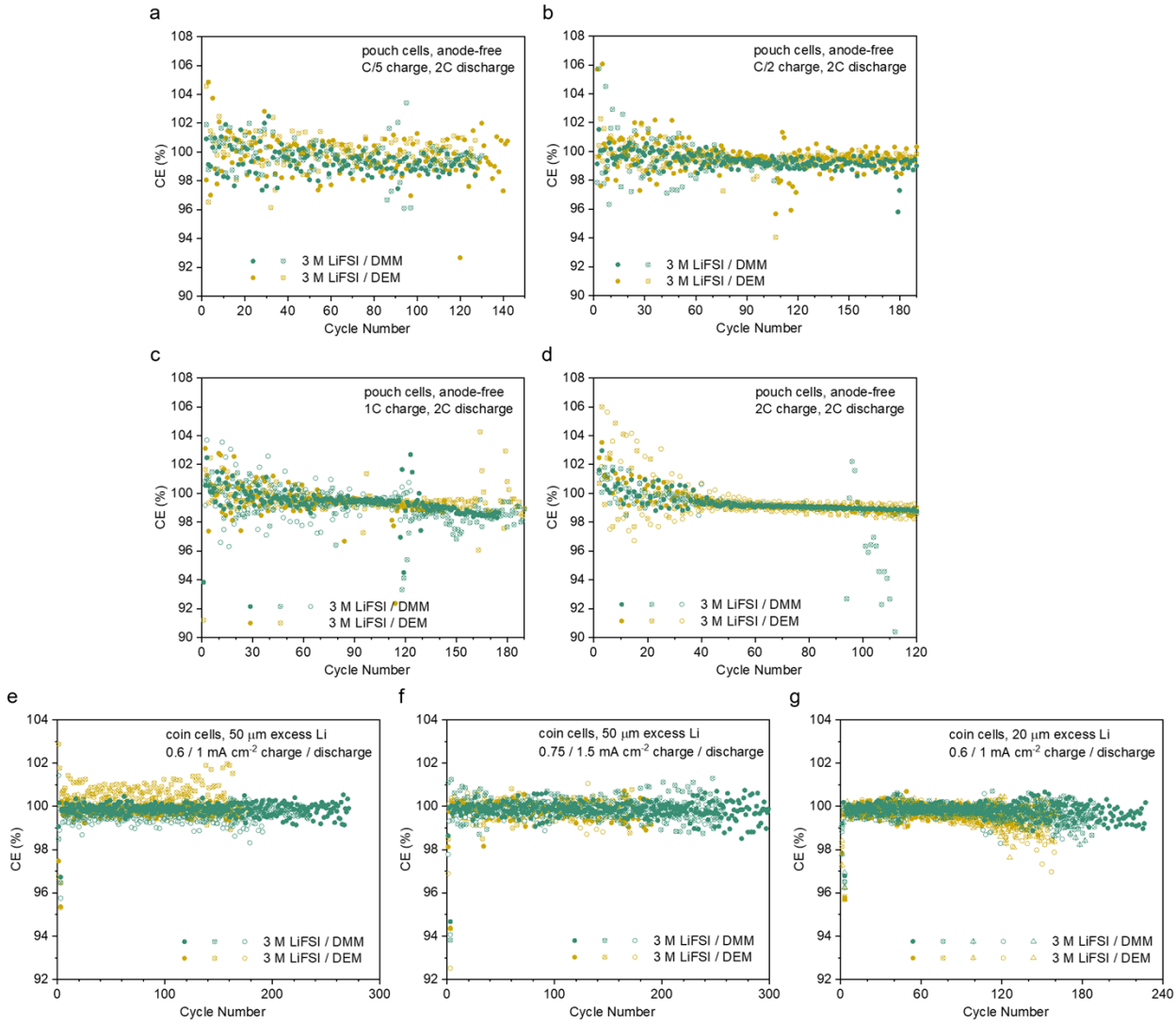

Figure S16. Corresponding CE values of cells in Figure 5.

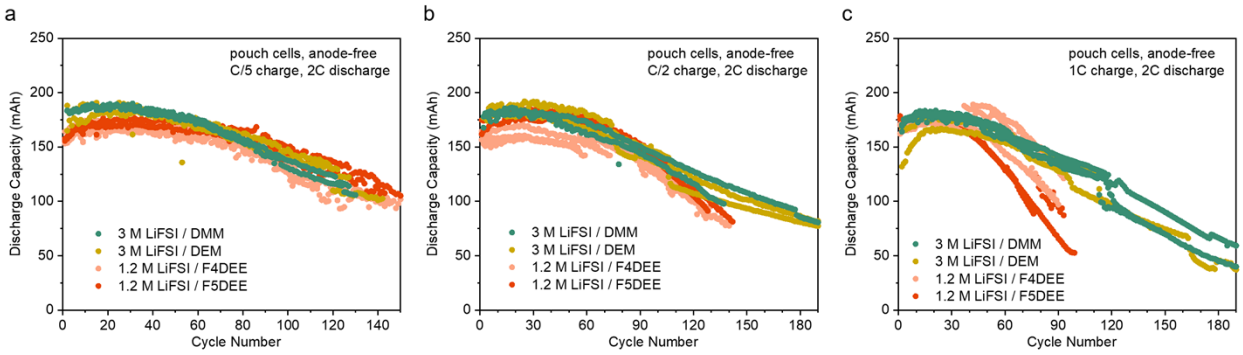

Figure S17. Direct comparison of FDEE electrolytes with DMM and DEM electrolytes in Cu||micro-LFP pouch cells. The data of FDEE were reproduced from ref [11].

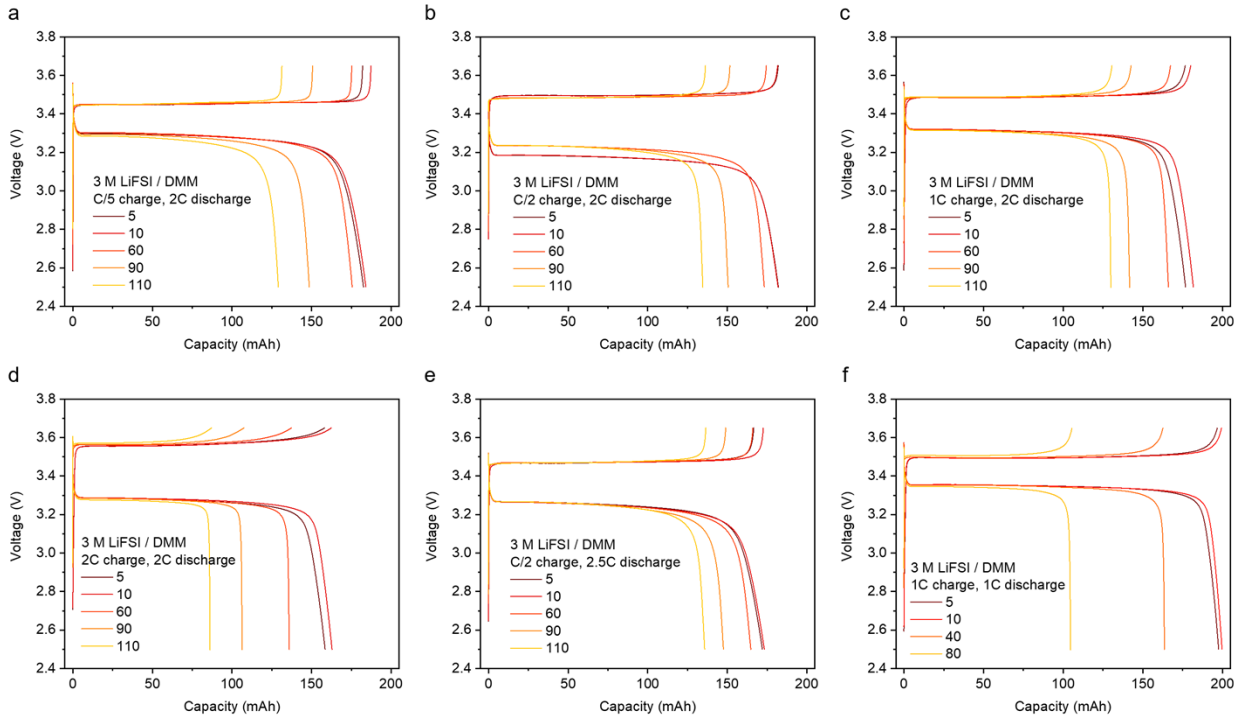

Figure S18. Voltage curves of anode-free Cu||micro-LFP pouch cells cycled at various charge and discharge rates in 3 M LiFSI / DMM.

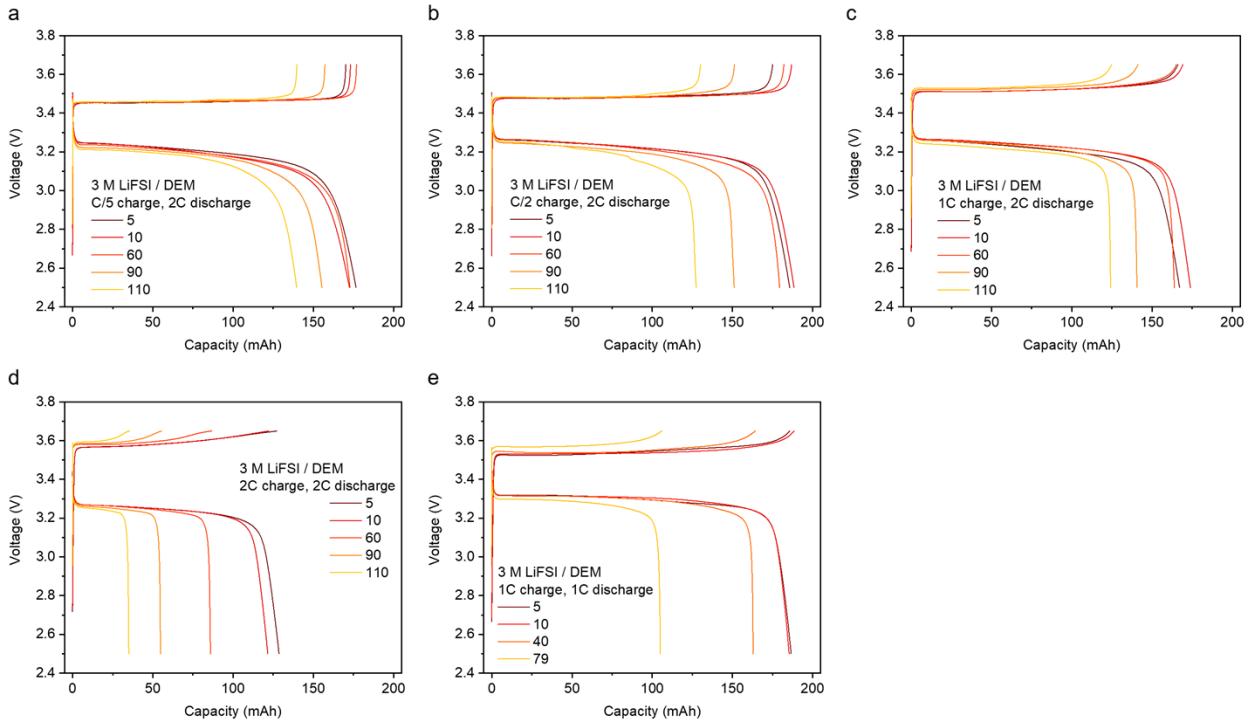

Figure S19. Voltage curves of anode-free Cu||micro-LFP pouch cells cycled at various charge and discharge rates in 3 M LiFSI / DEM.

Despite the differences in bulk and interfacial ion transport, the capacity utilization was similar in 3 M LiFSI / DMM and 3 M LiFSI / DEM at ≤1C charge rate (2 mA cm^{-2}) due to the flat voltage curve of LFP cells—a cut-off voltage of 3.65 V was sufficient to accommodate the overpotential (Figure S18a-c and S19a-c). In contrast, at 2C charge rate, the voltage divergence at the end of charge was obscured by overpotential, which led to the strong dependence of capacity utilization on overpotential (Figure S18d and S19d).

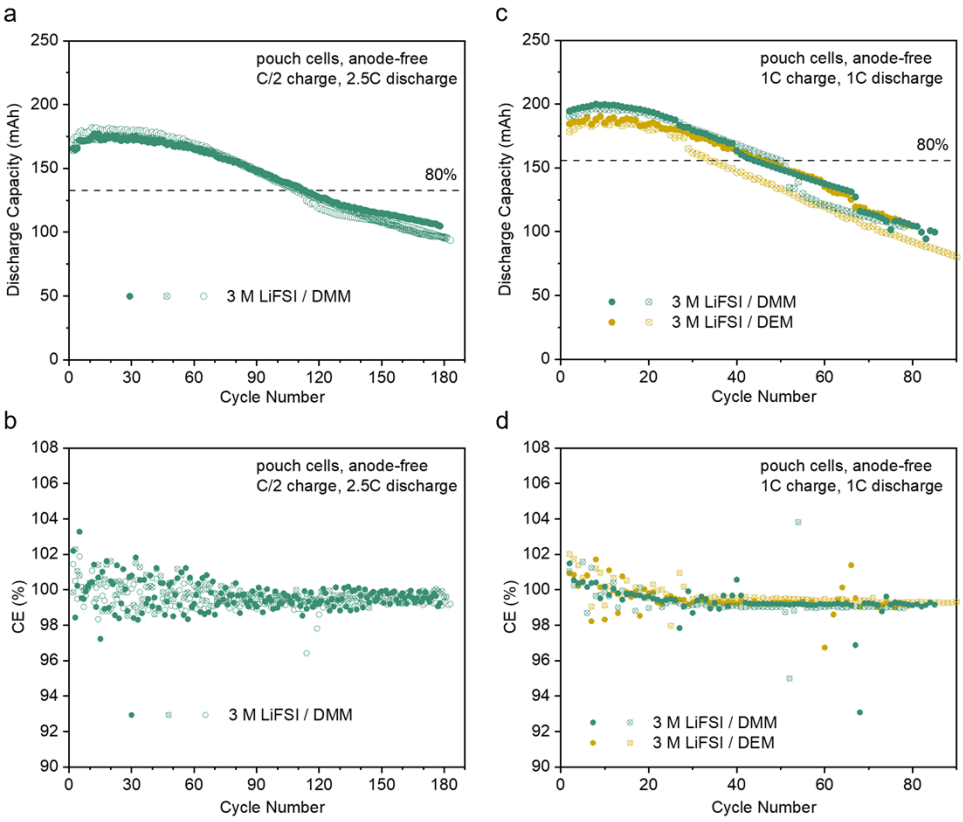

Figure S20. Anode-free Cu||micro-LFP pouch cells (nominally ~210 mAh, ~2.1 mAh cm^{-2}, 2.5 to 3.65 V, 0.5 mL electrolyte, 1C = 200 mA) cycled at various rates (the first-cycle charge was at C/10) with 3 M LiFSI / DMM and 3 M LiFSI / DEM. The data for every attempted cell are shown in Supplementary Figure S38.

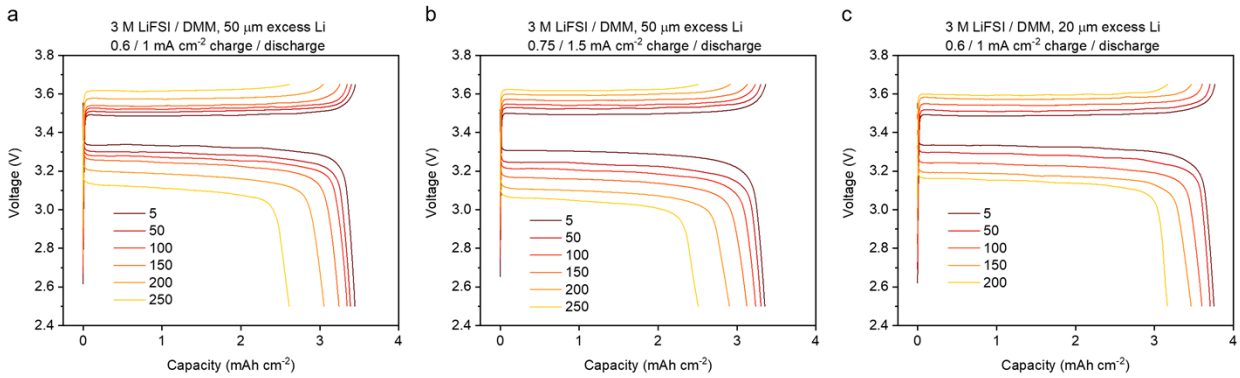

Figure S21. Voltage curves of thin-Li||micro-LFP coin cells cycled at various charge and discharge current densities in 3 M LiFSI / DMM.

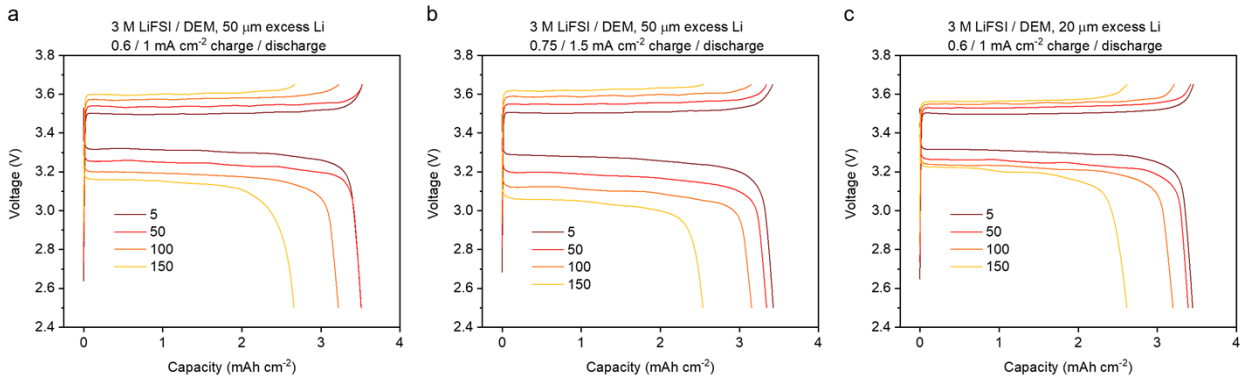

Figure S22. Voltage curves of thin-Li||micro-LFP coin cells cycled at various charge and discharge current densities in 3 M LiFSI / DEM.

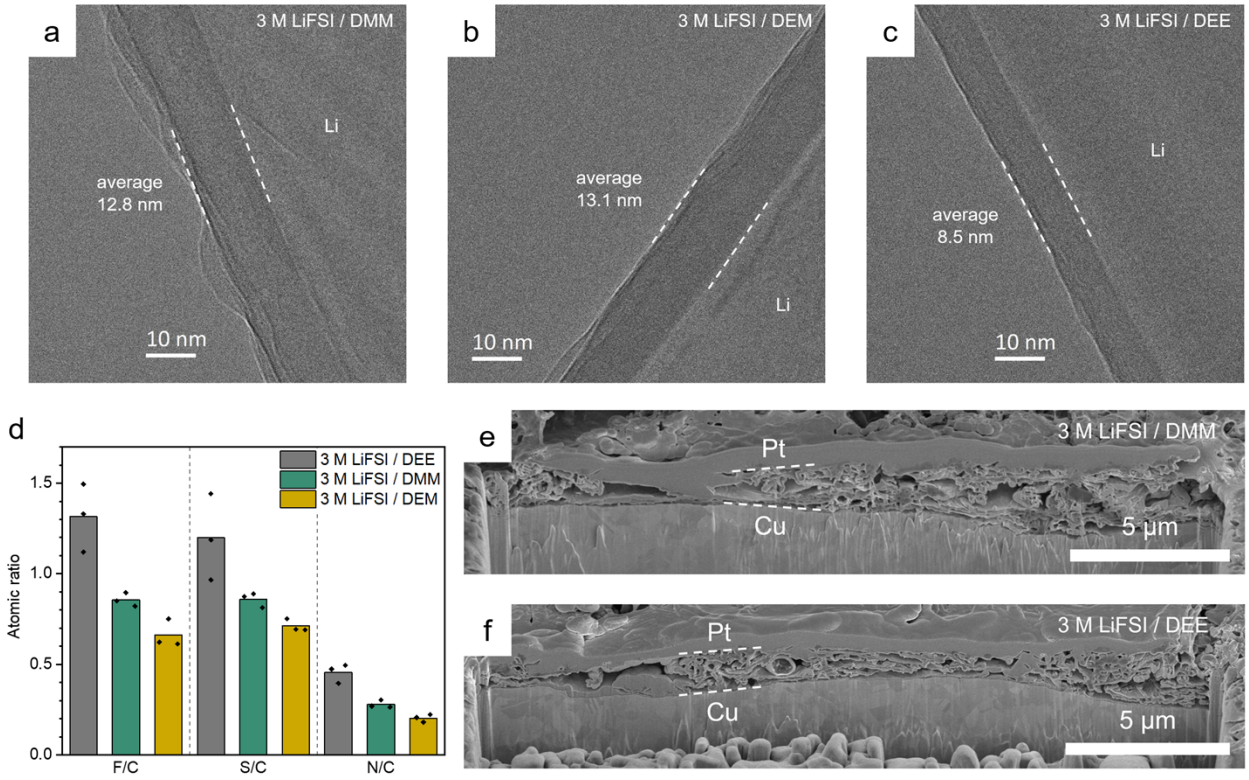

Figure S23. SEI properties in various nonfluorinated electrolytes. (a-c) Cryo-TEM images of SEI formed in 3 M LiFSI / DMM (a), DEM (b), and DEE (c). The average thickness was calculated from 10 measurements, and additional images are provided (Figure S24). (d) Atomic ratios by cryo-EDS comparing salt-derived (F, S, N) and solvent-derived (C) elements in the SEI. Three spots were measured for each sample, and the bar graphs represent their average. Oxygen was not included due to potential contamination from ice. (e-f) Cross-section FIB-SEM images of the rSEI structure formed in 3 M LiFSI / DMM (e) and DEE (f). Li||Cu cells were cycled at 0.5 mA cm^{-2} and 1 mAh cm^{-2} for 10 cycles. The active Li was stripped in the final step, leaving rSEI on Cu substrate. Pt was deposited to preserve the top surface of rSEI. Additional images are provided in Supplementary Figure S29.

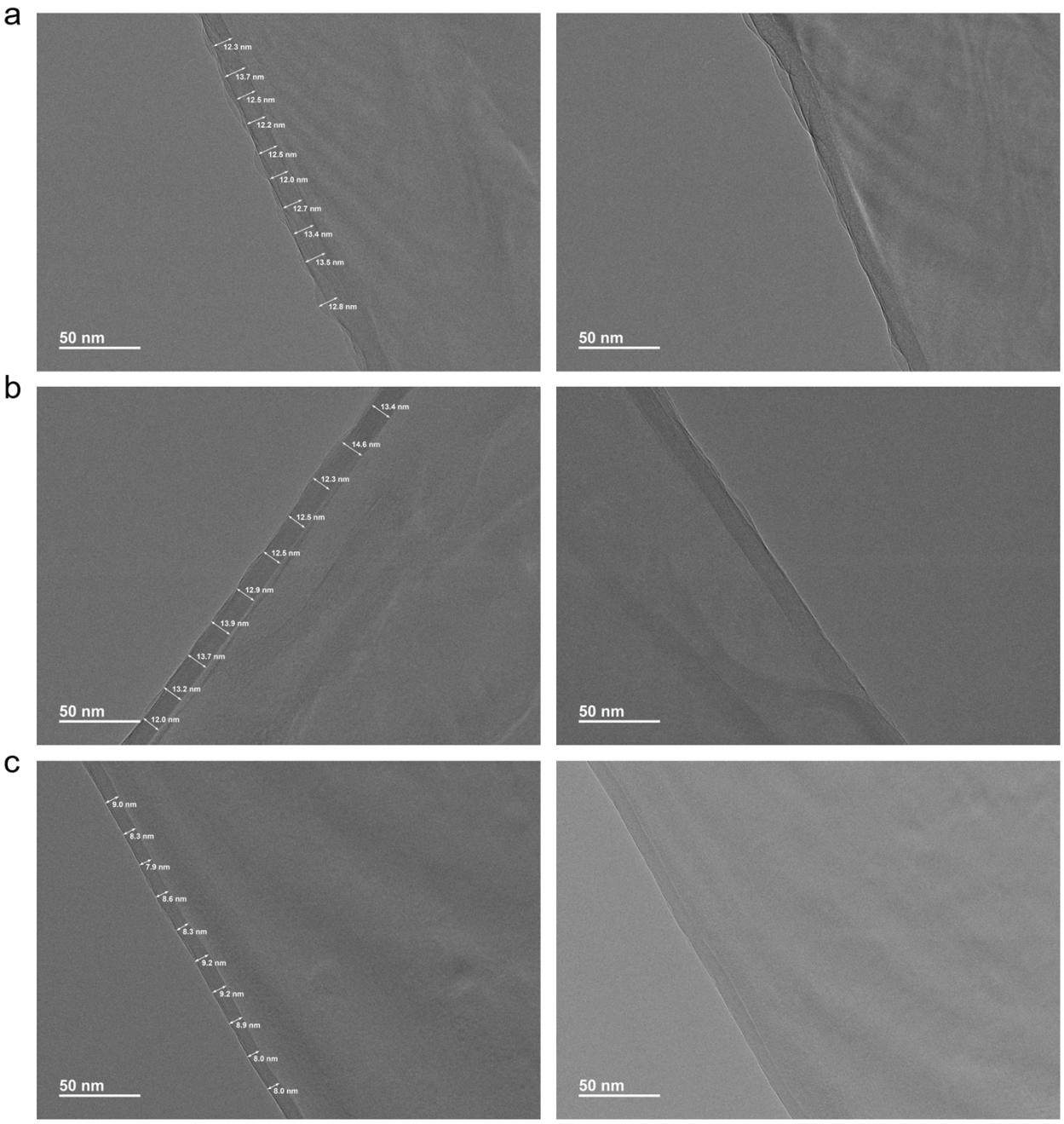

Figure S24. Cryo-TEM images of SEI formed in (a) 3 M LiFSI / DMM, (b) 3 M LiFSI / DEM, and (c) 3 M LiFSI / DEE. The left images show 10 measurements of SEI thickness. Additional images are provided on the right.

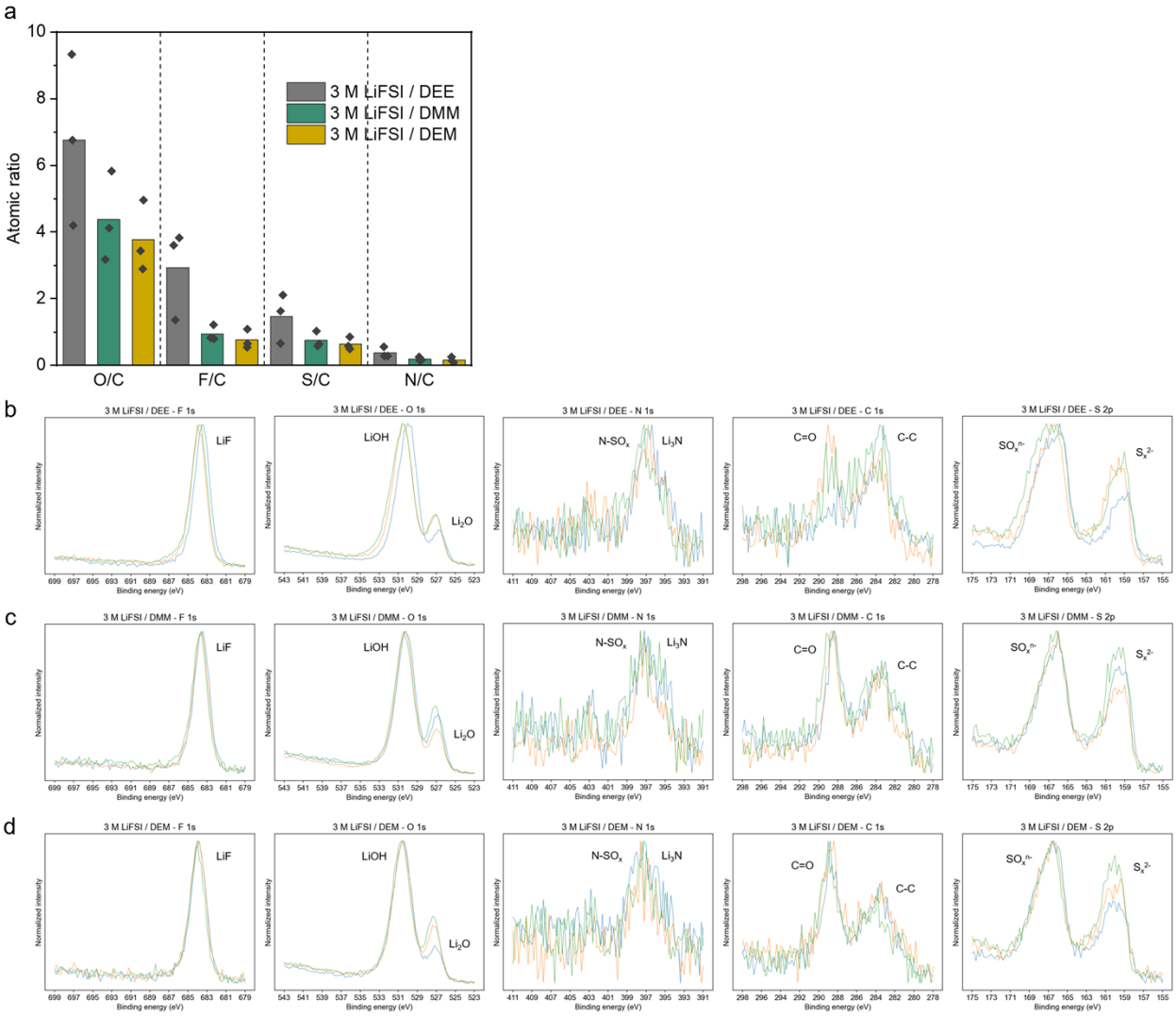

Figure S25. SEI compositions measured by XPS. For each sample, three random spots were characterized. (a) Atomic ratios. The bars represent average of three spots. (b) XPS spectra. Each colored trace represents a different spot. Li||Cu cells were first pre-conditioned at 0.2 mA cm^{-2} between 0 and 1 V for 10 cycles, followed by 10 cycles at 0.5 mA cm^{-2} plating for 1 mAh cm^{-2} and 0.5 mA cm^{-2} stripping to 1 V. After active Li was stripped from Cu, the rSEI was characterized.

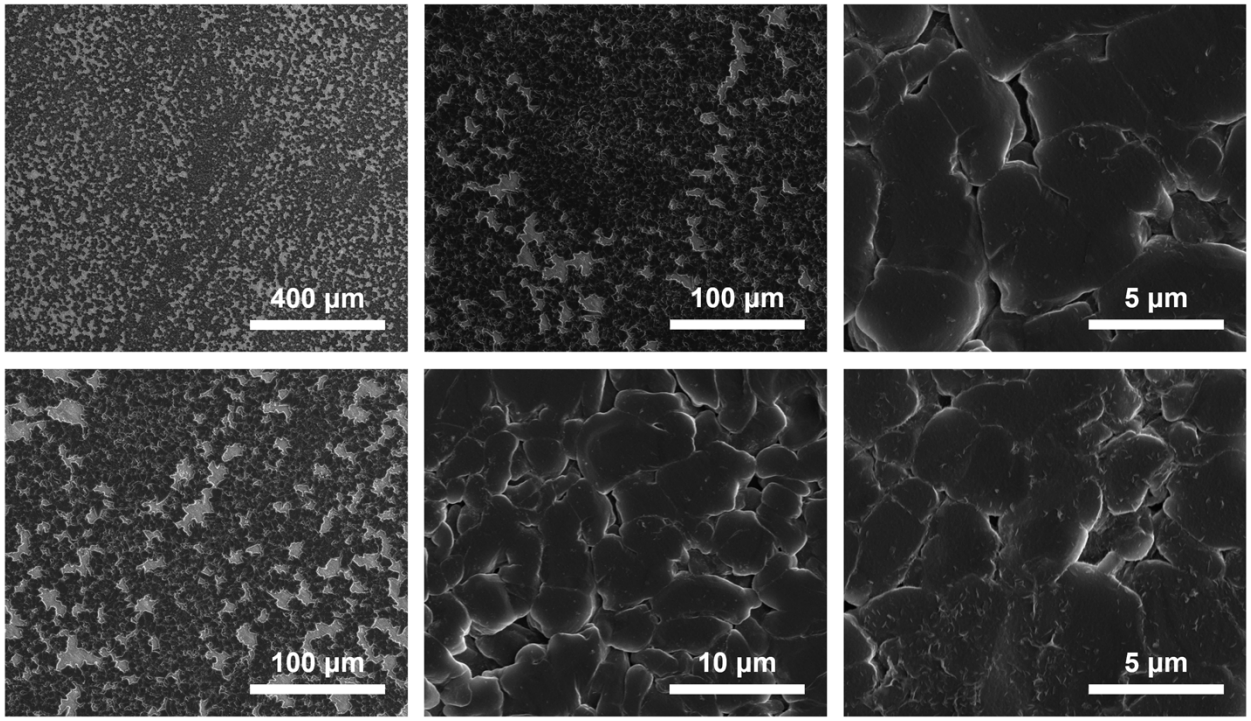

Figure S26. SEM images of the initial Li deposition morphology in 3 M LiFSI in DMM. A small amount of Li (0.5 mAh cm^{-2}) was plated onto Cu at 0.5 mA cm^{-2} in an uncycled Li||Cu cell.

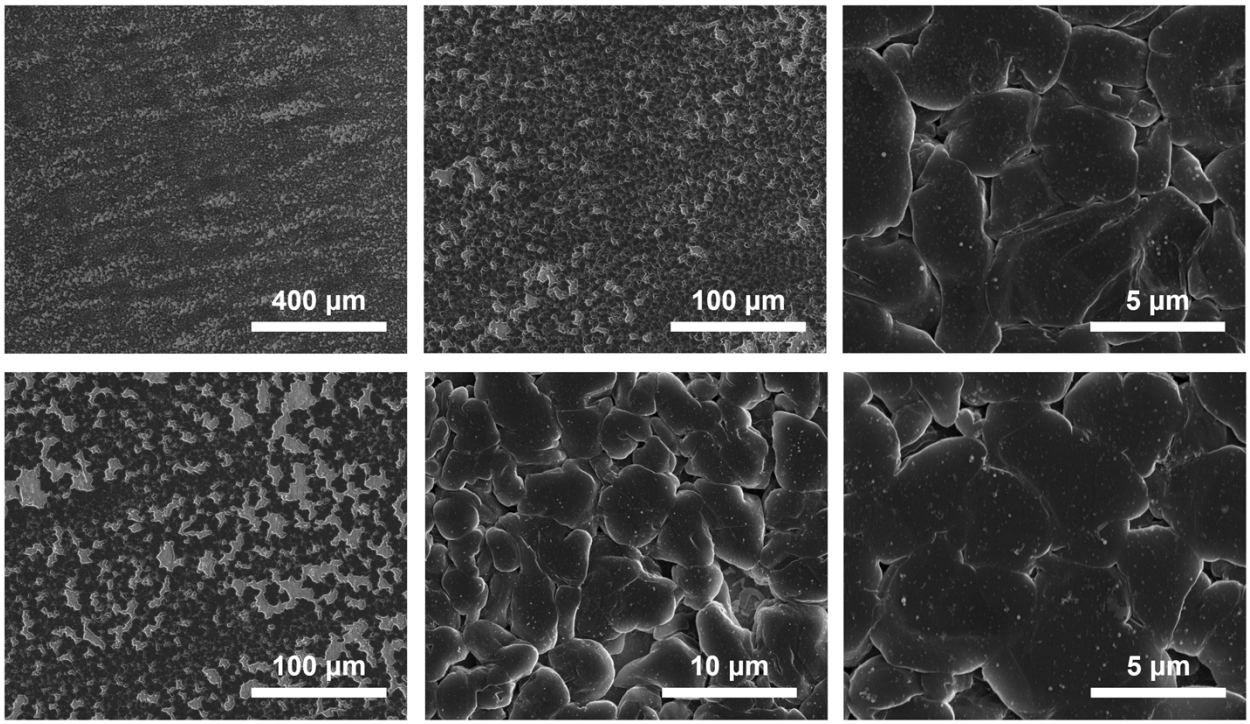

Figure S27. SEM images of the initial Li deposition morphology in 3 M LiFSI in DEM. A small amount of Li (0.5 mAh cm^{-2}) was plated onto Cu at 0.5 mA cm^{-2} in an uncycled Li||Cu cell.

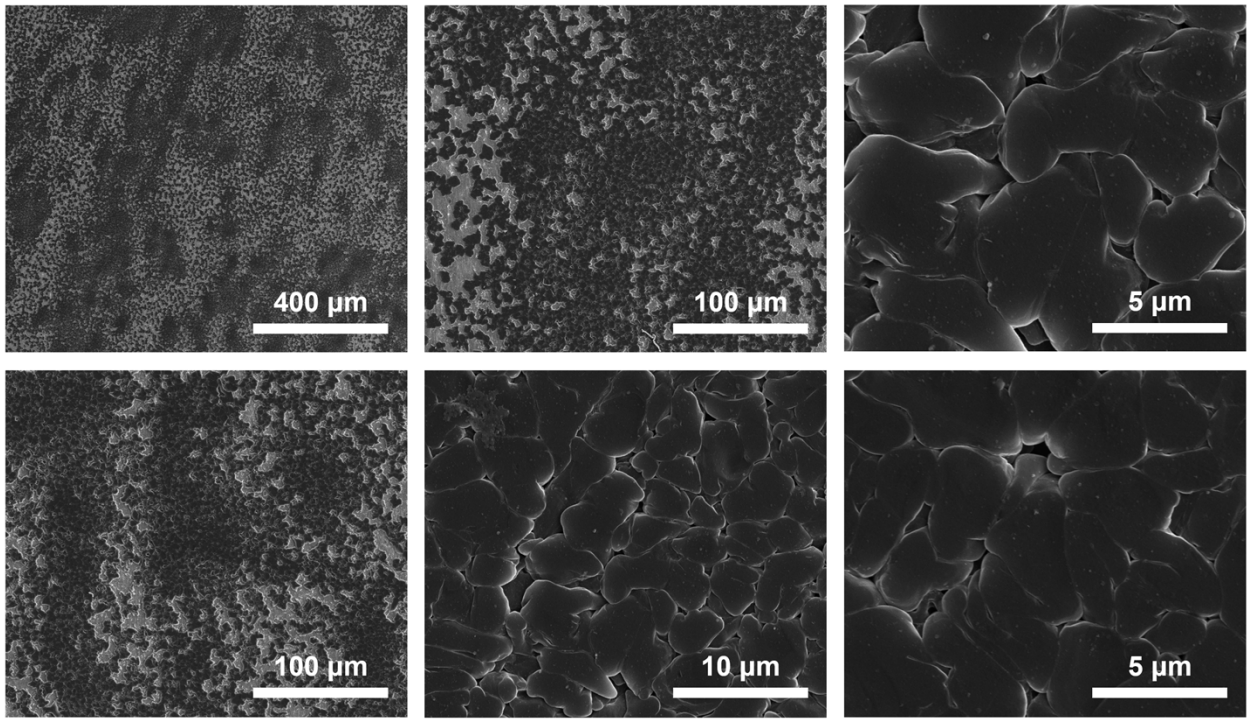

Figure S28. SEM images of the initial Li deposition morphology in 3 M LiFSI in DEE. A small amount of Li (0.5 mAh cm^{-2}) was plated onto Cu at 0.5 mA cm^{-2} in an uncycled Li||Cu cell.

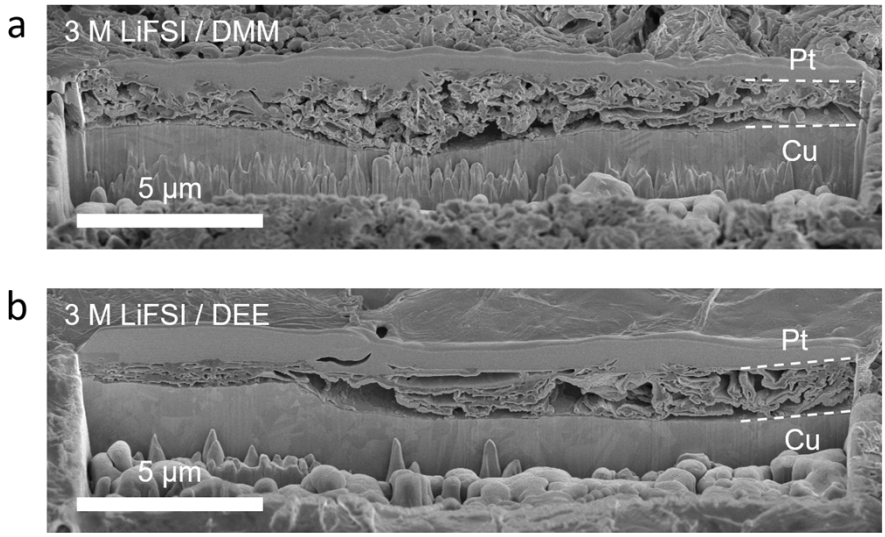

Figure S29. Cross-section FIB-SEM images of the rSEI structure formed after 10 cycles at 0.5 mA cm^{-2} and 1 mAh cm^{-2} in Li||Cu cells with 3 M LiFSI / DMM (a) and DEE (b). These are additional images to supplement Figure S23e-f.

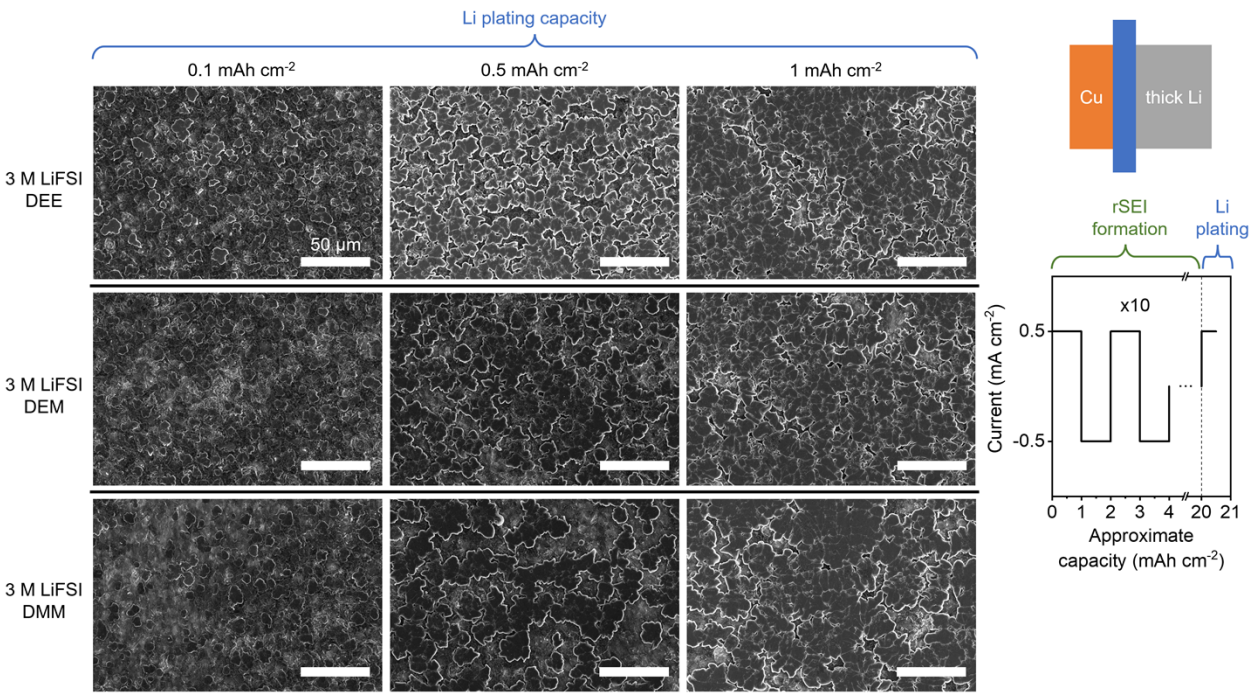

Figure S30. SEM images of Li and rSEI morphology on Cu electrode in various electrolytes. The cells were pre-conditioned at 0.2 mA cm^{-2} between 0 and 1 V for 10 cycles, followed by 10 cycles at 0.5 mA cm^{-2} and 1 mAh cm^{-2} plating and 0.5 mA cm^{-2} stripping to 1 V to form rSEI. In the final step, 0.1, 0.5 or 1 mAh cm^{-2} capacity was plated at 0.5 mA cm^{-2}. The applied current profiles are shown on the right. The capacities of final Li plating are labeled by columns on the top. The electrolytes are labeled by rows on the left. The scale bars are 50 µm.

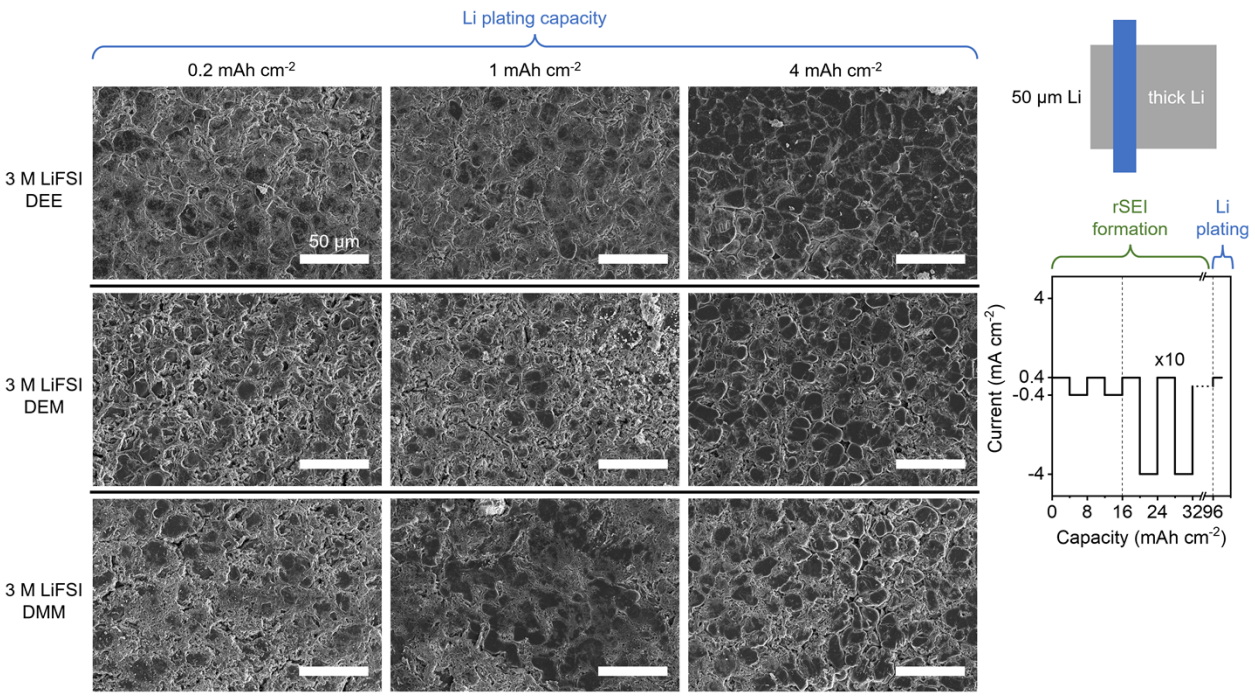

Figure S31. SEM images of Li and rSEI morphology on 50 μm Li electrode in various electrolytes. The cells were pre-cycled at 0.4 mA cm^{-2} for 2 cycles, followed by 10 cycles at 0.4 mA cm^{-2} plating and 4 mA cm^{-2} stripping, with 4 mAh cm^{-2} in each step to form rSEI. In the final step, 0.2, 1 or 4 mAh cm^{-2} capacity was plated at 0.4 mA cm^{-2}. The applied current profiles are shown on the right. The capacities of final Li plating are labeled by columns on the top. The electrolytes are labeled by rows on the left. The scale bars are 50 μm.

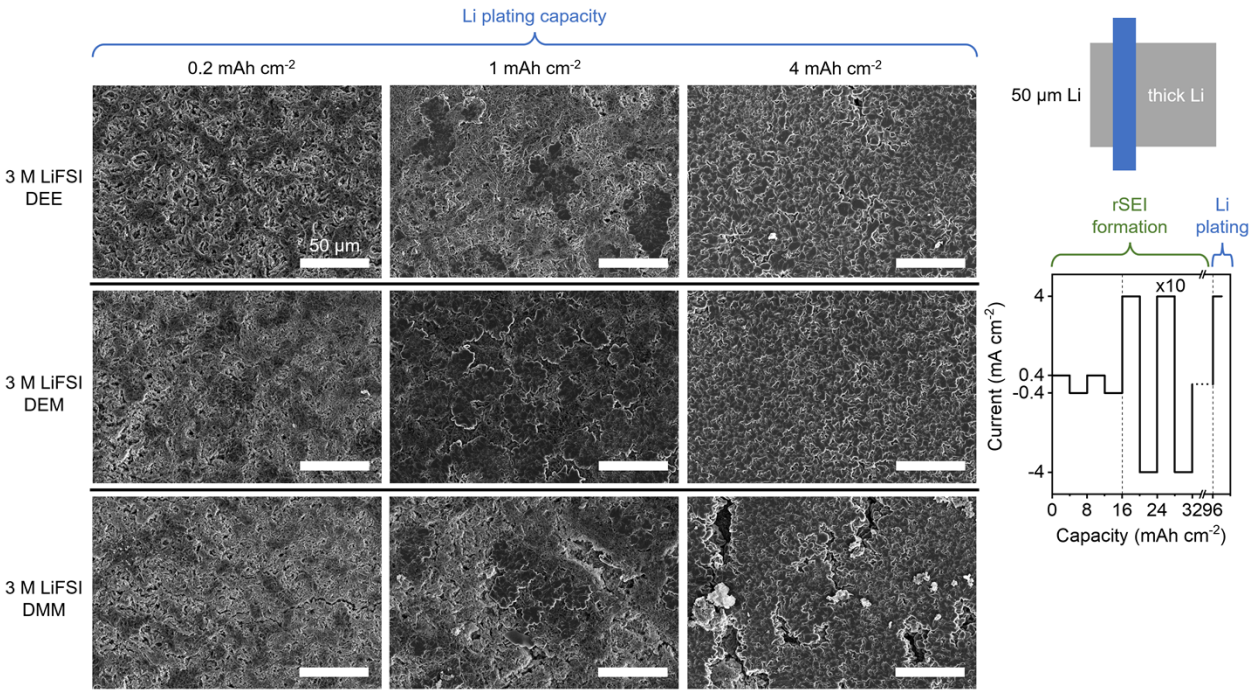

Figure S32. SEM images of Li and rSEI morphology on 50 µm Li electrode in various electrolytes. The cells were pre-cycled at 0.4 mA cm^{-2} for 2 cycles, followed by 10 cycles at 4 mA cm^{-2}, with 4 mAh cm^{-2} in each step to form rSEI. In the final step, 0.2, 1 or 4 mAh cm^{-2} capacity was plated at 4 mA cm^{-2}. The applied current profiles are shown on the right. The capacities of final Li plating are labeled by columns on the top. The electrolytes are labeled by rows on the left. The scale bars are 50 µm.

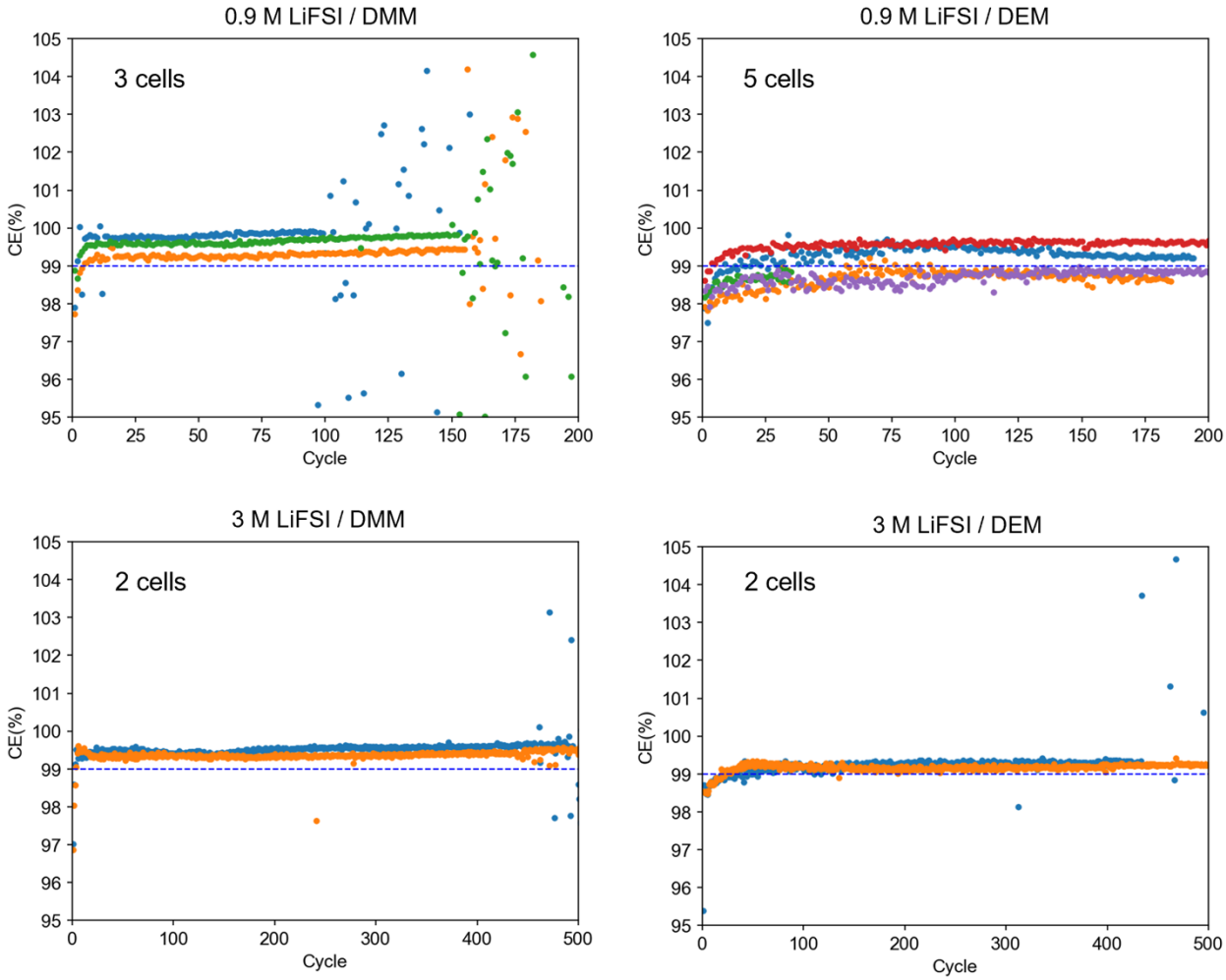

Figure S33. Every Li||Cu cell attempted for Figure 3a, b.

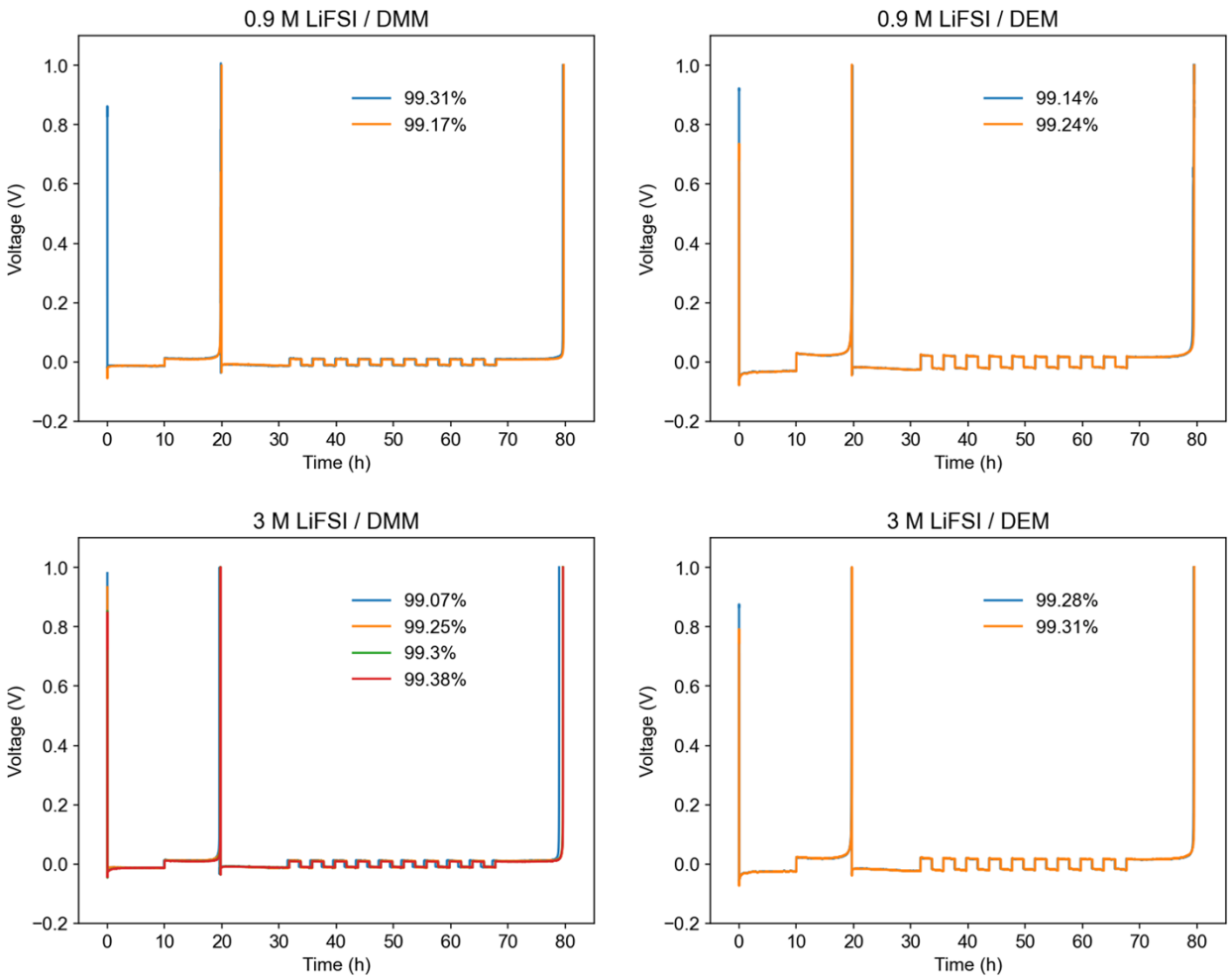

Figure S34. Every Li||Cu cell attempted for Figure 3c.

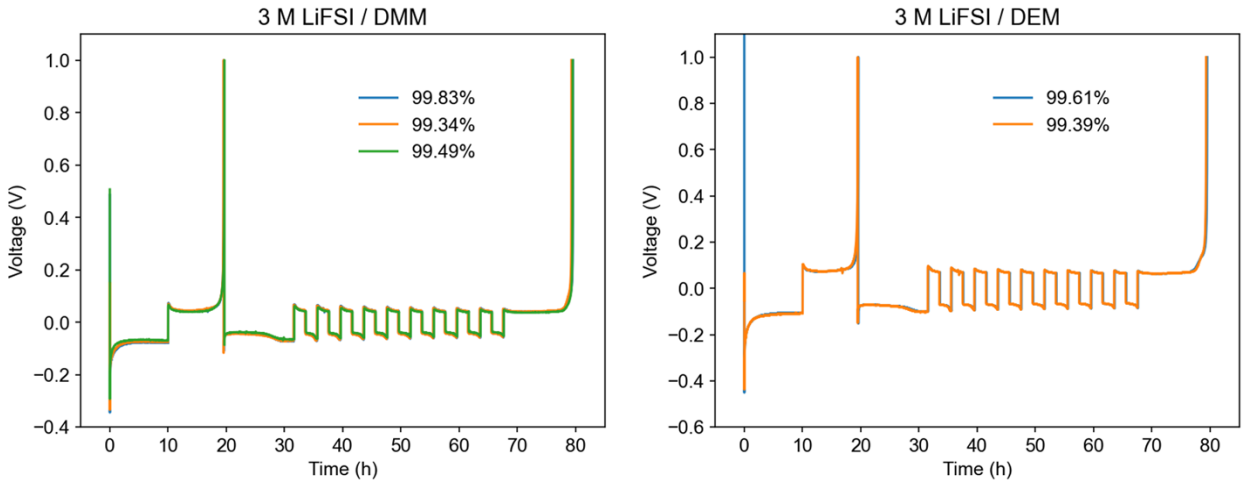

Figure S35. Every Li||Cu cell attempted for Figure 3d.

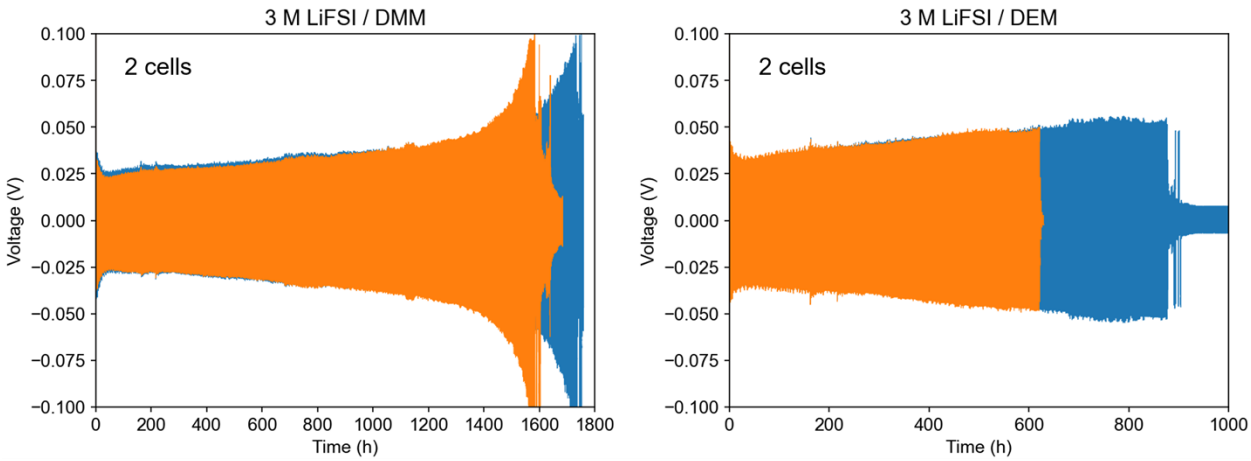

Figure S36. Every Li||Li cell attempted for Figure 4a.

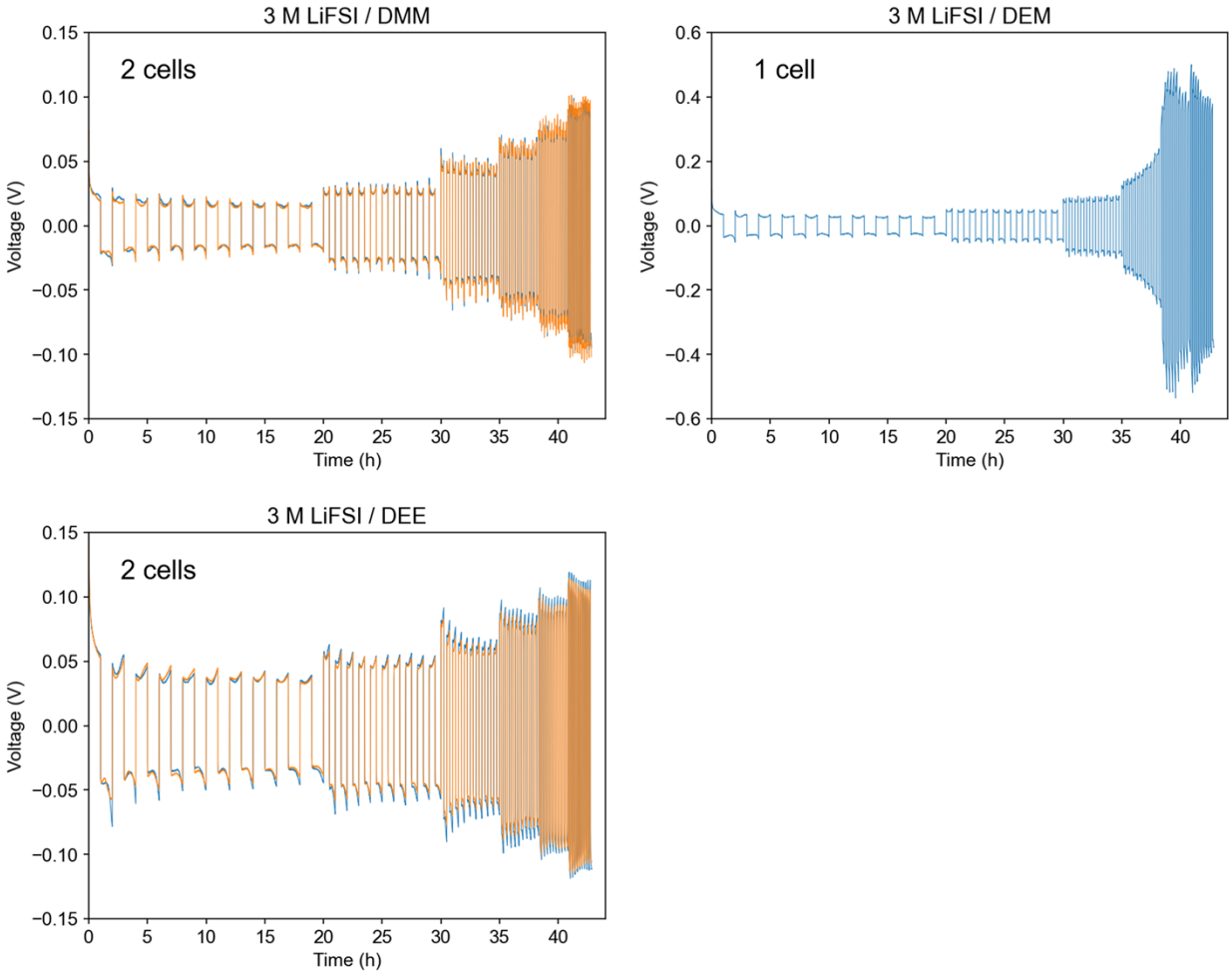

Figure S37. Every Li||Li cell attempted for Figure 4b.

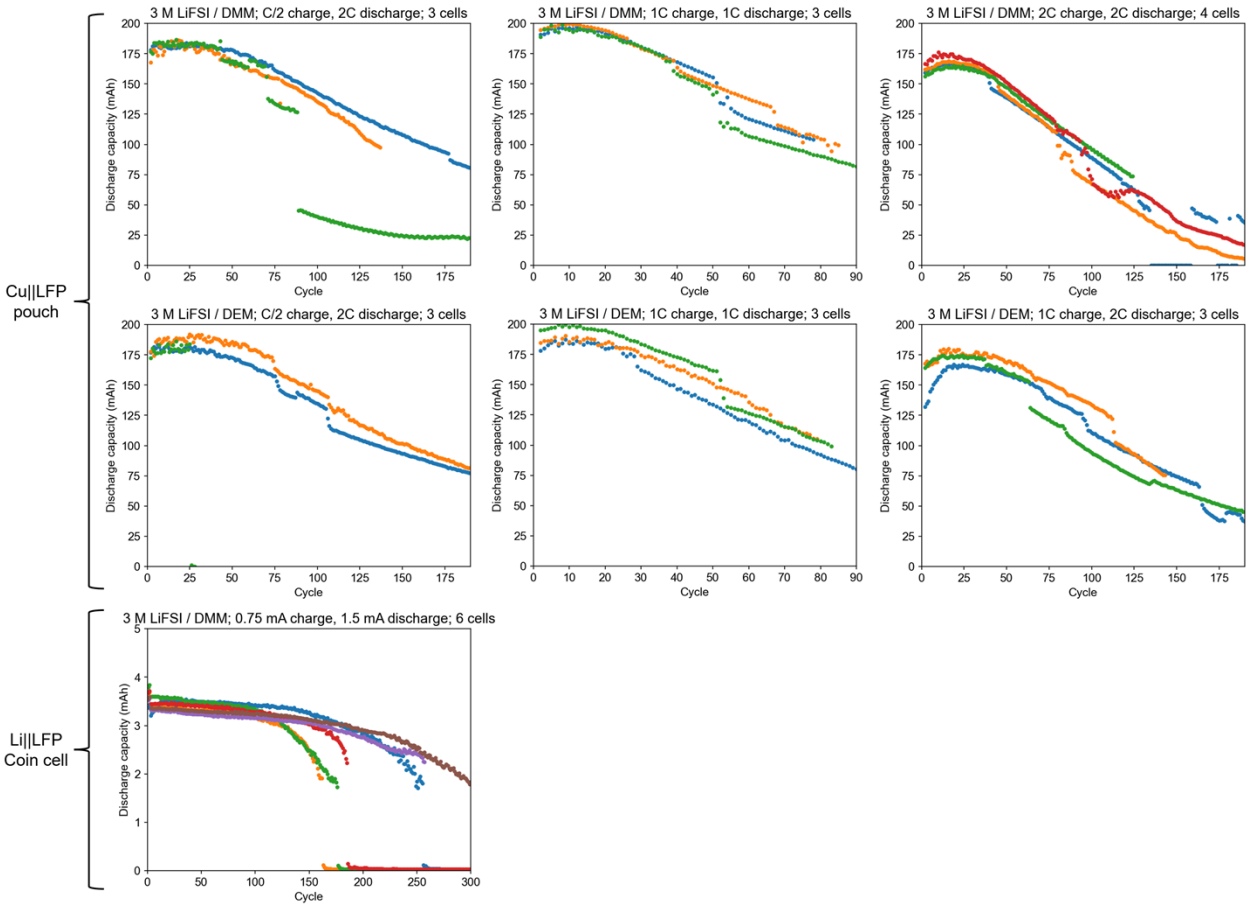

Figure S38. Every Cu||LFP pouch cell and Li||LFP coin cell attempted for Figure 5b, c, d, f, and Figure S20c. For the rest of Figure 5 and Figure S20, all attempted cells are included.

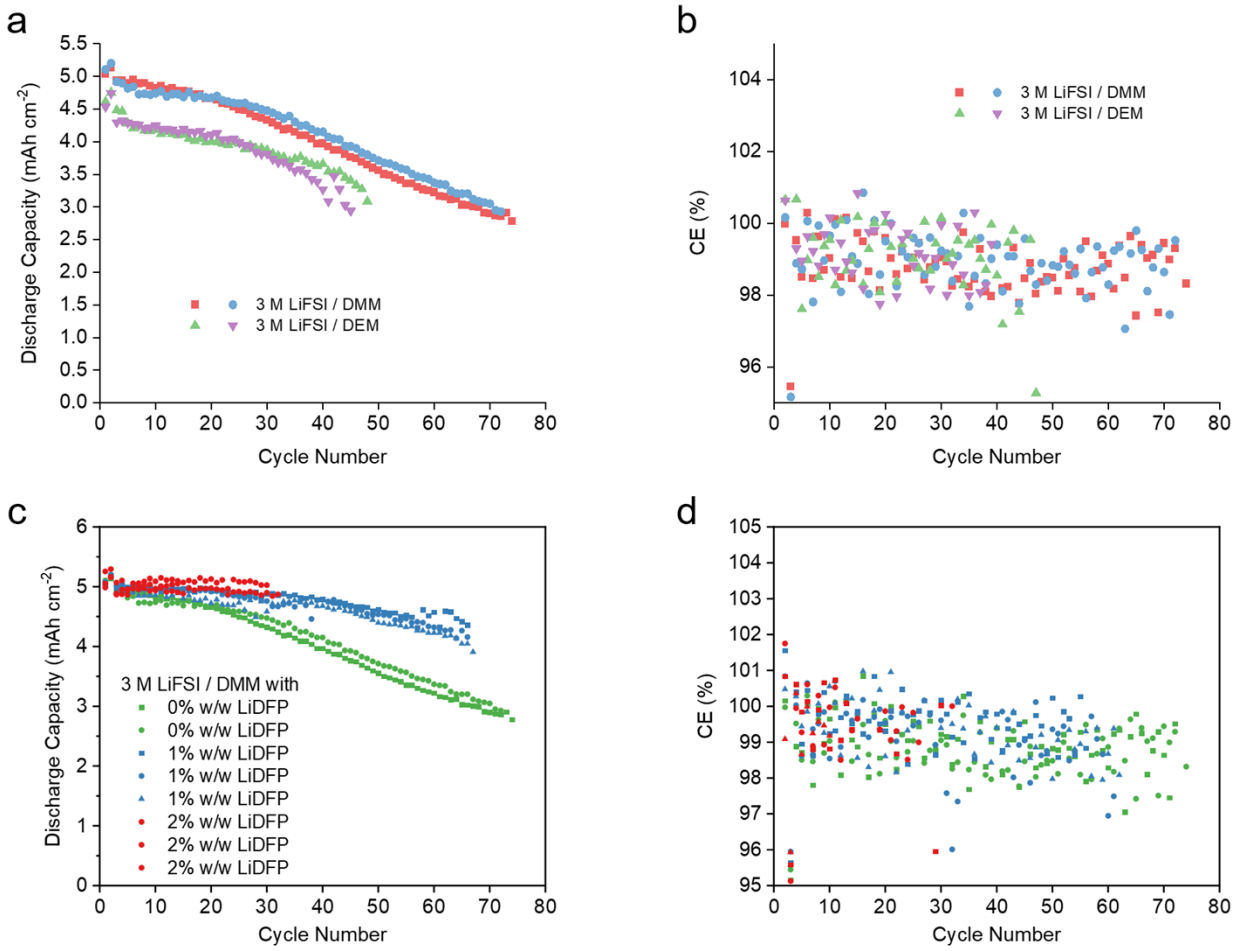

Figure S39. Cycle stability of acetal electrolytes in 50 µm Li||5 mAh cm^{-2} NMC811 coin cells. The cells were cycled at 0.8/1.3 mA cm^{-2} charge/discharge within 2.8-4.4 V. (a) Discharge capacity and (b) CE in 3 M LiFSI / DMM and DEM. (c) Discharge capacity and (d) CE in 3 M LiFSI / DMM with 0-2% LiDFP to improve NMC811 stability.

When applying 3 M LiFSI / DMM and DEM to Li||NMC811 cells, the capacity quickly decayed (Figure S39a). The CE of these cells remained below 100% (Figure S39b) despite excess Li metal at the anode, which indicated irreversible loss at the cathode. Therefore, the short cycle life can be attributed to the poor oxidative stability of the acetal electrolytes. $LiPO_2F_2$ (LiDFP) has been shown as an effective cathode additive.[24] By adding 1-2% LiDFP to 3 M LiFSI/ DMM, the cycle stability of Li||NMC811 cells was further improved (Figure S39c-d). This offers additional evidence that the cycle life was limited by cathode stability due to electrolyte oxidation.

References

(1) Carey, F. A.; Sundberg, R. J. *Advanced Organic Chemistry*, 5th ed.; Springer: New York, 2007.

(2) Abe, A.; Inomata, K.; Tanisawa, E.; Ando, I. Conformation and Conformational Energies of Dimethoxymethane and 1,1-Dimethoxyethane. *J. Mol. Struct.* **1990**, *238*, 315–323.

(3) Anderson, J. E.; Heki, K.; Hirota, M.; Jørgensen, F. S. Setting the Anomeric Effect against Steric Effects in Simple Acyclic Acetals. Non-Anomeric Non-Classical Conformations. An N.M.R. and Molecular Mechanics Investigation. *J. Chem. Soc. Chem. Commun.* **1987**, No. 8, 554–555. https://doi.org/10.1039/C39870000554.

(4) Chen, Y.; Yu, Z.; Gong, H.; Zhang, W.; Rudnicki, P.; Huang, Z.; Yu, W.; Kim, S. C.; Boyle, D. T.; Sayavong, P.; et al. Failure Process During Fast Charging of Lithium Metal Batteries with 2 Weakly Solvating Fluoroether Electrolytes. *J. Phys. Chem. C* **2024**. https://doi.org/10.1021/acs.jpcc.4c01740.

(5) Giffin, G. A. The Role of Concentration in Electrolyte Solutions for Non-Aqueous Lithium-Based Batteries. *Nat. Commun.* **2022**, *13*, 5250. https://doi.org/10.1038/s41467-022-32794-z.

(6) Borodin, O.; Self, J.; Persson, K. A.; Wang, C.; Xu, K. Uncharted Waters: Super-Concentrated Electrolytes. *Joule* **2020**, *4* (1), 69–100. https://doi.org/10.1016/j.joule.2019.12.007.

(7) Yamada, Y.; Wang, J.; Ko, S.; Watanabe, E.; Yamada, A. Advances and Issues in Developing Salt-Concentrated Battery Electrolytes. *Nat. Energy* **2019**, *4* (4), 269–280. https://doi.org/10.1038/s41560-019-0336-z.

(8) Boyle, D. T.; Kong, X.; Pei, A.; Rudnicki, P. E.; Shi, F.; Huang, W.; Bao, Z.; Qin, J.; Cui, Y. Transient Voltammetry with Ultramicroelectrodes Reveals the Electron Transfer Kinetics of Lithium Metal Anodes. *ACS Energy Lett.* **2020**, *5* (3), 701–709. https://doi.org/10.1021/acsenergylett.0c00031.

(9) Zhang, Z.; Li, Y.; Xu, R.; Zhou, W.; Li, Y.; Oyakhire, S. T.; Wu, Y.; Xu, J.; Wang, H.; Yu, Z.; et al. Capturing the Swelling of Solid-Electrolyte Interphase in Lithium Metal Batteries. *Science (80-.).* **2022**, *375* (6576), 66–70. https://doi.org/10.1126/science.abi8703.

(10) Li, Y.; Li, Y.; Pei, A.; Yan, K.; Sun, Y.; Wu, C. L.; Joubert, L. M.; Chin, R.; Koh, A. L.; Yu, Y.; et al. Atomic Structure of Sensitive Battery Materials and Interfaces Revealed by Cryo–Electron Microscopy. *Science (80-.).* **2017**, *358* (6362), 506–510. https://doi.org/10.1126/science.aam6014.

(11) Yu, Z.; Rudnicki, P. E.; Zhang, Z.; Huang, Z.; Celik, H.; Oyakhire, S. T.; Chen, Y.; Kong, X.; Kim, S. C.; Xiao, X.; et al. Rational Solvent Molecule Tuning for High-Performance Lithium Metal Battery Electrolytes. *Nat. Energy* **2022**, *7* (1), 94–106. https://doi.org/10.1038/s41560-021-00962-y.

(12) Yu, Z.; Wang, H.; Kong, X.; Huang, W.; Tsao, Y.; Mackanic, D. G.; Wang, K.; Wang, X.; Huang, W.; Choudhury, S.; et al. Molecular Design for Electrolyte Solvents Enabling Energy-Dense and Long-Cycling Lithium Metal Batteries. *Nat. Energy* **2020**, *5* (7), 526–533. https://doi.org/10.1038/s41560-020-0634-5.

(13) Wang, J.; Huang, W.; Pei, A.; Li, Y.; Shi, F.; Yu, X.; Cui, Y. Improving Cyclability of Li Metal Batteries at Elevated Temperatures and Its Origin Revealed by Cryo-Electron Microscopy. *Nat. Energy* **2019**, *4*, 664–670. https://doi.org/10.1038/s41560-019-0413-3.

(14) Li, M.; Zhang, Q.; Yang, X.; Zhu, Y.; Cheng, Y.; Shen, S.; Gu, M. Deciphering the Mechanism of Concentrated Electrolyte for Lithium Metal Anode via Cryogenic Electron Microscopy. *J. Power Sources* **2023**, *557* (August 2022), 232543. https://doi.org/10.1016/j.jpowsour.2022.232543.

(15) Fan, X.; Chen, L.; Borodin, O.; Ji, X.; Chen, J.; Hou, S.; Deng, T.; Zheng, J.; Yang, C.; Liou, S. C.; et al. Non-Flammable Electrolyte Enables Li-Metal Batteries with Aggressive Cathode Chemistries. *Nat. Nanotechnol.* **2018**, *13* (8), 715. https://doi.org/10.1038/s41565-018-0183-2.

(16) Ren, X.; Zou, L.; Cao, X.; Engelhard, M. H.; Liu, W.; Burton, S. D.; Lee, H.; Niu, C.; Matthews, B. E.; Zhu, Z.; et al. Enabling High-Voltage Lithium-Metal Batteries under Practical Conditions. *Joule* **2019**, *3* (7), 1662–1676. https://doi.org/10.1016/j.joule.2019.05.006.

(17) Cao, X.; Ren, X.; Zou, L.; Engelhard, M. H.; Huang, W.; Wang, H.; Matthews, B. E.; Lee, H.; Niu, C.; Arey, B. W.; et al. Monolithic Solid–Electrolyte Interphases Formed in Fluorinated Orthoformate-Based Electrolytes Minimize Li Depletion and Pulverization. *Nat. Energy* **2019**, *4* (9), 796–805. https://doi.org/10.1038/s41560-019-0464-5.

(18) Xue, W.; Huang, M.; Li, Y.; Zhu, Y. G.; Gao, R.; Xiao, X.; Zhang, W.; Li, S.; Xu, G.; Yu, Y.; et al. Ultra-High-Voltage Ni-Rich Layered Cathodes in Practical Li Metal Batteries Enabled by a Sulfonamide-Based Electrolyte. *Nat. Energy* **2021**, *6* (5), 495–505. https://doi.org/10.1038/s41560-021-00792-y.

(19) Chen, Y.; Yu, Z.; Rudnicki, P.; Gong, H.; Huang, Z.; Kim, S. C.; Lai, J. C.; Kong, X.; Qin, J.; Cui, Y.; et al. Steric Effect Tuned Ion Solvation Enabling Stable Cycling of High-Voltage Lithium Metal Battery. *J. Am. Chem. Soc.* **2021**, *143* (44), 18703–18713. https://doi.org/10.1021/jacs.1c09006.

(20) Wang, H.; Huang, W.; Yu, Z.; Huang, W.; Xu, R.; Zhang, Z.; Bao, Z.; Cui, Y. Efficient Lithium Metal Cycling over a Wide Range of Pressures from an Anion-Derived Solid-Electrolyte Interphase Framework. *ACS Energy Lett.* **2021**, *6*, 816–825. https://doi.org/10.1021/acsenergylett.0c02533.

(21) Wang, H.; Kim, S. C.; Rojas, T.; Zhu, Y.; Li, Y.; Ma, L.; Xu, K.; Ngo, A. T.; Cui, Y. Correlating Li-Ion Solvation Structures and Electrode Potential Temperature Coefficients. *J. Am. Chem. Soc.* **2021**, *143* (5), 2264–2271. https://doi.org/10.1021/jacs.0c10587.

(22) Adams, B. D.; Zheng, J.; Ren, X.; Xu, W.; Zhang, J. G. Accurate Determination of Coulombic Efficiency for Lithium Metal Anodes and Lithium Metal Batteries. *Adv. Energy Mater.* **2018**, *8* (7), 1–11. https://doi.org/10.1002/aenm.201702097.

(23) Chen, Y.; Yu, Z.; Rudnicki, P.; Gong, H.; Huang, Z.; Kim, S. C.; Lai, J.-C.; Kong, X.; Qin, J.; Cui, Y.; et al. Steric Effect Tuned Ion Solvation Enabling Stable Cycling of High-Voltage Lithium Metal Battery. *J. Am. Chem. Soc.* **2021**, *143* (44), 18703–18713. https://doi.org/10.1021/jacs.1c09006.

(24) Tan, S.; Shadike, Z.; Li, J.; Wang, X.; Yang, Y.; Lin, R.; Cresce, A.; Hu, J.; Hunt, A.; Waluyo, I.; et al. Additive Engineering for Robust Interphases to Stabilize High-Ni Layered Structures at Ultra-High Voltage of 4.8 V. *Nat. Energy* **2022**, *7* (6), 484–494. https://doi.org/10.1038/s41560-022-01020-x.